ABSTRACT

Title of thesis: CO TOLERANCE OF NANO-ARCHITECTURED
PT-MO ANODE ELECTROCATALYSTS
FOR PEM FUEL CELL SYSTEMS

Jennifer Ezu Hu, Master of Science, 2009

Directed by: Associate Professor Gregory Jackson
Department of Mechanical Engineering

Enhanced CO tolerance of PEM fuel cell anode electrocatalysts is essential for improving the performance of PEM fuel cell systems operating with hydrocarbon reformers. This work explores the CO tolerance of PEM fuel cell membrane electrode assemblies (MEAs) fabricated with two promising nano-architectured Pt-Mo anode electrocatalysts — $Pt_{0.8}Mo_{0.2}$ alloy and MoO_x@Pt core-shell catalysts — which demonstrated extremely high CO tolerance in previous thin-film electrode studies. By holding all other MEA components (cathode catalyst, electrolyte membrane, and supporting gas diffusion layers) constant, polarization tests in pure H_2 and H_2 streams contaminated with up to 1000 ppm CO provided a basis for assessing the relative CO tolerance of the catalysts. Anode electrocatalyst stability was also investigated by operating the MEAs in 100 ppm CO over several days. Commercial and in-house fabricated MEAs with a conventional anode catalyst were used for comparison. $Pt_{0.8}Mo_{0.2}$ demonstrated the highest performance in CO, with a voltage drop of only 95 mV in 100 ppm CO at 0.5 $A{\cdot}cm^{-2}$, compared to drops of 230 mV for PtRu and 260 mV for the core-shell electrocatalyst. However, the MoO_x@Pt electrochemical performance, with its reduced Pt content, was comparable to the highly active PtMo electrocatalyst for CO concentrations below 50 ppm on a per gram of precious metal basis, and preliminary stability studies indicate that the core-shell structure may also provide protection against detrimental Mo leaching in the acidic electrolyte. Both Mo-containing catalysts were poorly utilized, perhaps owing to residual surface contamination from the synthesis procedures, suggesting that their performance could be significantly improved with further optimization of fabrication procedures.

A system-level model was also used to explore the impact of current-day and potential advances in CO tolerant electrocatalysts on the system performance of a PEM fuel cell system operating in conjunction with a hydrocarbon autothermal reformer and a preferential CO oxidation (PROx) reactor for CO clean-up. Empirical models of CO tolerant fuel cell performance were based on experimental data obtained with the PtMo alloy tested in the experimental portion of this study. As CO tolerance was increased, system efficiencies improved primarily at conditions where the fuel cell stack operated at high current densities, and the improvement is largely to higher fuel cell voltages and to a lesser extent to reductions in parasitic loads. Furthermore, increased fuel cell CO tolerance permitted significantly lower PROx CO selectivities and CO conversions without the significant penalties in overall system efficiency observed with the present-day CO tolerance of Pt alloy electrocatalysts.

CO Tolerance of Nano-architectured Pt-Mo Anode Electrocatalysts for PEM Fuel Cell Systems

by

Jennifer Ezu Hu

Thesis submitted to the Faculty of the Graduate School of the
University of Maryland, College Park in partial fulfillment
of the requirements for the degree of
Master of Science
2009

Advisory Committee:
Professor Gregory Jackson, Chair/Advisor
Professor Bryan Eichhorn
Professor Michael Zachariah

Acknowledgments

Many people contributed to this work and this document, and are greatly deserving of recognition and thanks.

First, my adviser, Dr. Greg Jackson, who was encouraging through many setbacks and always pushed me towards a deeper understanding of PEM fuel cells and the underlying electrochemistry. Many thanks also go to Zhufang Liu, whose catalyst synthesis and characterization formed the basis for this work. He and Dr. Bryan Eichhorn also provided valuable advice and expertise throughout the project. Dr. Chunsheng Wang and his students allowed me to use their hot press, and seeing their lights on in the neighboring lab was a comfort on many weekends and late nights. Larry Lai in the NISPLab provided assistance with the SEM imaging and EDX. This work was sponsored by the Army Research Office, as part of a project also involving Ballard Power Systems. Pat Hearn, Chris Tesluk, and the rest of the Ballard group at UMD also contributed to many helpful discussions, and their work on the 5 kW PEMFC generator was an inspiring reminder that even basic catalyst research can grow up into real systems.

Atul Bhargav, Steven DeCaluwe, Rick Stroman, Siddharth Patel, Josh Pearlman, and the entire Jackson group were great friends in and out of lab, patiently supplying staples and explanations of the Butler-Volmer equation the many many times that I needed them. I'd like to thank my friends and housemates who have made DC home, as well as more geographically distant friends who all managed to convey encouragement when I needed it, even without Facebook. Matt Malinowski

and Jessica Lee contributed significantly to my vegetable consumption over the last two years, and Headley Jacobus was always there to help eat. I'm also grateful for the many cross-country pep talks and wake-up calls from Ankur Mehta, Amittai Axelrod, and Michael Pihulic that kept me on track and moving forward. Special thanks to my editors, Jeff Erickson, Michael Pihulic, and Kenny Hu, and finally, to my parents for all of their support over the years.

Table of Contents

List of Tables

List of Figures

List of Abbreviations

Symbols

A_{cell}	geometric area of single electrochemical cell in fuel cell stack / cm^2
F	Faraday's constant = 96548 C·gmol electrons^{-1}
G	Gibbs free energy
$h_{H_2,comb}$	lower enthalpy of combustion of H_2 / J·kg^{-1}
$h_{HC,comb}$	lower enthalpy of combustion of hydrocarbon / J·kg^{-1}
i	average effective current density per unit geometric area in the fuel cell stack / A·cm^{-2}
i^0	exchange current density / A·cm^2
i'	mass specific current
$\dot{m}_{H_2,anode\ in}$	mass flow rate of H_2 into the fuel cell anode / kg·s^{-1}
$\dot{m}_{HC,in}$	mass flow rate of hydrocarbon into fuel reformer / kg·s^{-1}
n_{cells}	number of cells in the fuel cell stack
n_{el}	number of moles of electrons involved in a chemical reaction
O/C	oxygen (from O_2) to carbon (from fuel) atomic ratio in fuel reformer inlet
R	ideal gas constant
S/C	steam to carbon (from fuel) ratio in fuel reformer inlet
T_{amb}	ambient temperature / °C
T_{WGS}	water-gas-shift reactor outlet temperature / °C
UA	overall heat transfer coefficient
V_{cell}	voltage across an individual electrochemical cell in fuel cell stack / V
V_{rev}	reversible voltage calculated by Nernst equation, equivalent to open circuit voltage / V
$\bar{W}_{H_2}$	molecular weight of H_2 / g·gmol^{-1}
$\dot{W}_{lost}$	parasitic loads
$\dot{W}_{net}$	net electrical power output / W

ε_{H_2}	fraction of anode inlet H_2 utilized in stack
η_{act}	activation overpotential
η_{BOP}	balance of plant efficiency
η_{CO}	effective CO overpotential
η_{conc}	concentration or mass transport overpotential
η_{ohm}	ohmic overpotential
η_{FC}	fuel cell subsystem efficiency
η_{FP}	fuel processor subsystem efficiency
η_{th}	thermal (total system) efficiency
ξ_{CO}	CO tolerance factor

Acronyms

ATR	autothermal reformer
BOP	balance of plant
CCM	catalyst-coated membrane (method of membrane electrode assembly fabrication)
CV	cyclic voltammetry
DFT	density functional theory
EDX	energy-dispersive X-ray spectroscopy (also EDS)
EIS	electrochemical impedance spectroscopy
FC	fuel cell
FRT	fiberglass-reinforced Teflon
GDE	gas diffusion electrode, formed by applying a catalyst layer on a gas diffusion layer
GDL	gas diffusion layer
HOR	hydrogen oxidation reaction
ICP-MS	inductively coupled plasma mass spectrometry
IPA	isopropyl alcohol / isopropanol
MEA	membrane electrode assembly
NAA	neutron activation analysis

OCV	open circuit (reversible) voltage
ORR	oxygen reduction reaction
PEM	proton exchange membrane or polymer electrolyte membrane
PFA	perfluoroalkoxy, fluoropolymer used as gasket material
PM	precious metal
PROx	preferential oxidation (of CO)
PVP	polyvinylpyrrolidone
RDE	rotating disk electrode
SEM	scanning electron microscope
TEM	transmission electron microscope
TGA	thermogravimetic analysis
WGS	water-gas-shift (reaction or reactor)
XPS	X-ray photoelectron spectroscopy
XRD	X-ray diffraction

Chapter 1

Introduction

Fuel cells are currently being developed for many different applications, including portable and stationary power generation, forklifts, buses, and cars. One of the primary obstacles to widespread adoption of fuel cells is access to H_2 fuel, which presents challenges both in terms of the large volumes required due to the low energy density of H_2, and the current lack of infrastructure for H_2 distribution and storage. Although direct methanol and ethanol fuel cells (DMFCs and DEFCs) are being developed to run directly on liquid alcohols with relatively high energy densities, and high-temperature solid-oxide fuel cells (SOFCs) with hydrocarbon fuel flexibility are being demonstrated, these each present their own challenges and cannot match the high power densities of low-temperature polymer electrolyte membrane (PEM) fuel cells operating on pure H_2.

Thus, in order to capture the benefits of high-power H_2 performance while avoiding the logistics of obtaining H_2, in many PEM fuel cell applications H_2 is produced at the point of use by breaking down hydrocarbons in a process known as reforming. Hydrocarbons are advantageous in their abundance, high energy density and ease of transport. They also have the potential to come from renewable sources such as biomass. Regardless of the source of the hydrocarbon, the products of reformation include CO and CO_2 in addition to H_2. Because CO in the feed stream severely degrades the power output of low-temperature PEM fuel cells employing Pt catalysts, significant research efforts are being made to develop strategies to mitigate this CO poisoning effect.

This investigation is conducted in conjunction with efforts to demonstrate a working prototype of a liquid hydrocarbon-fueled PEM fuel cell generator system with integrated reformer at the University of Maryland in collaboration with Ballard Power Systems. The performance and design of such systems, as well as their eventual commercial viability, could benefit greatly from CO tolerant fuel cell stacks incorporating catalysts resistant to CO poisoning. This study investigates the CO tolerance of two promising Pt-Mo electrocatalysts, and also models the effects of enhanced CO tolerance on PEM fuel systems fueled with hydrocarbons.

1.1 PEM Fuel Cell Systems

1.1.1 Principles of PEM Fuel Cell Operation

There are many types of fuel cells that are made from various materials and operate on different fuels; this study focuses on low-temperature polymer electrolyte membrane (PEM) fuel cells. PEM fuel cells consume H_2 and O_2 and produce water and electricity. They consist of an anode and a cathode, separated by a proton-conducting and electrically-insulating electrolyte. The basic operation of a PEM fuel cell is shown below in Figure 1.1. The overall reaction that takes place in the fuel cell is:

$$\mathrm{H}_2 + \frac{1}{2}\mathrm{O}_2 \rightarrow \mathrm{H}_2O. \tag{1.1}$$

The reaction is separated into two half-cell reactions that occur on the anode and cathode. On the anode, fuel (H_2) interacts with a catalyst and is split into protons and electrons. This hydrogen oxidation reaction (HOR) is shown in Reaction 1.2:

$$\mathrm{2H_2O}\ (el) + \mathrm{H_2}\ (g) \rightarrow \mathrm{2H_3O^+}\ (el) + 2e^-\ (anode) \tag{1.2}$$

where the labels in parentheses denote the phase of the reactant or product: (*el*) is the electrolyte and (*g*) is the gas phase. Protons from the oxidized H_2 cross the humidified membrane to the cathode in the form of hydronium (H_3O^+) ions, where another catalyst facilitates the oxygen reduction reaction (ORR),

$$\mathrm{2H_3O^+}\ (el) + 2e^-\ (cathode) + \frac{1}{2}\mathrm{O_2}\ (g) \rightarrow \mathrm{2H_2O}\ (el) + \mathrm{2H_2O}\ (cathode) \tag{1.3}$$

Because the membrane is electrically insulating, the electrons must travel through an external circuit, where they do work.

The driving force for the reaction is the reduction in free energy between the products and reactants of Reaction 1.1. The change in free energy without current load can be written as

$$\Delta G = n_{el} F V_{rev} \tag{1.4}$$

where n_{el} is the number of moles of electrons transferred in the reaction (in this case n_{el}=2), F is Faraday's constant, and V_{rev} is the thermodynamic reversible potential. V_{rev} can be calculated using the Nernst equation (shown here for Reaction 1.1):

$$V_{rev} = V^0 + \frac{RT}{n_{el}F} \ln\left(\frac{P_{H_2} P_{O_2}^{1/2}}{a_{H_2O}}\right) \tag{1.5}$$

where R is the ideal gas constant, T is the temperature, P_k is the partial pressure of species k, and a_{H_2O} is the activity of water. V^0 is the cell voltage at temperature

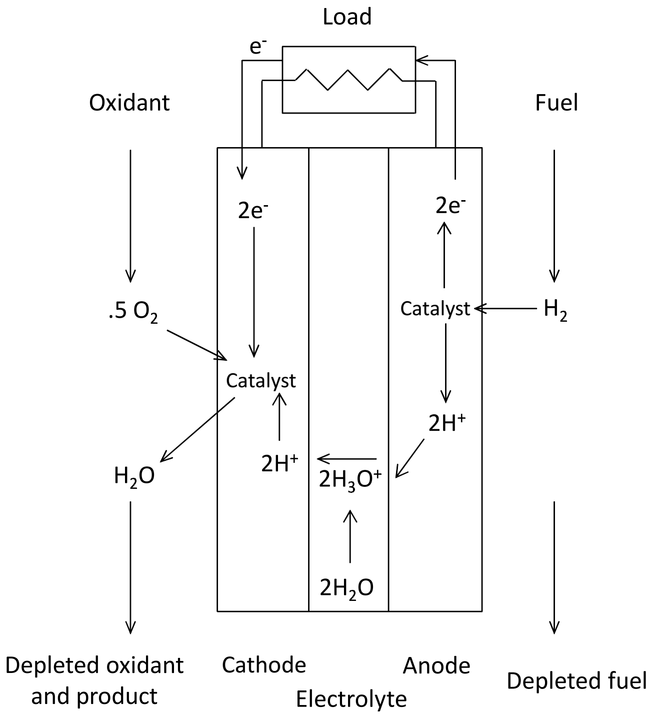

Figure 1.1: Basic operation of a PEM fuel cell with pure H_2 fuel.

T and activities of 1.0 for each species, and can be found by looking up ΔG^0 at standard temperature (298.15 K) from thermodynamic tables and substituting into

$$V^0 = \frac{\Delta G^0}{n_{el} F} = 1.23\ V. \tag{1.6}$$

V_{rev} from Equation 1.5 is the ideal potential — in practice measured voltages will be lower, mostly due to leakage across the membrane lowering partial pressures of the reactants. Equation 1.5 applies only at reversible conditions when no current is being drawn from the cell, so V_{rev} is also known as the open circuit voltage (OCV).

Irreversible losses that lower the actual cell voltage (V_{cell}) during operation at non-zero currents are called overpotentials and are denoted by η. Figure 1.2 shows a sample voltage-current (V-i) curve which plots V_{cell} as a function of current density (i), the current per unit geometric area of the electrodes. V_{cell} falls further from the ideal potential as current density increases due to three types of overpotentials: activation overpotentials (η_{act}), ohmic overpotentials (η_{ohm}), and concentration or mass transport overpotentials (η_{conc}).

Activation overpotentials dominate at low current densities, and represent the voltage penalties assessed for initiating a net charge transfer across each electrode-electrolyte interface. The oxidation reduction reaction has a much higher electrochemical activation barrier than the hydrogen oxidation reaction, thus activation overpotentials primarily occur on the cathode. η_{act} can be related to current density using a modified Butler-Volmer equation,

$$i = i^0 \left[\exp\left(\frac{\beta_f n_{el} F \eta_{act}}{RT} \right) - \exp\left(\frac{-\beta_r n_{el} F \eta_{act}}{RT} \right) \right]. \tag{1.7}$$

Here β_f and β_r are global charge transfer coefficients for the forward and reverse global, half cell reactions, and i^0 is the exchange current density, i.e., the rate of charge transfer in either direction. At OCV there is no net current because the forward and reverse reactions are in equilibrium; i^0 is an indicator of catalytic activity.

Ohmic overpotentials are a bulk measure of ionic and electronic resistances occurring within the electrodes and membrane, and at interfaces between components. Properly designed cells can minimize η_{ohm}, and it can easily be measured via impedance spectroscopy or via current-interruption. η_{ohm} is linear with current density:

$$\eta_{ohm} = i R_{ohm} \tag{1.8}$$

where R_{ohm} is the area specific resistance (ASR) of the cell. Finally, the concentration overpotential becomes significant at high current densities when pressure losses become rate-limiting.

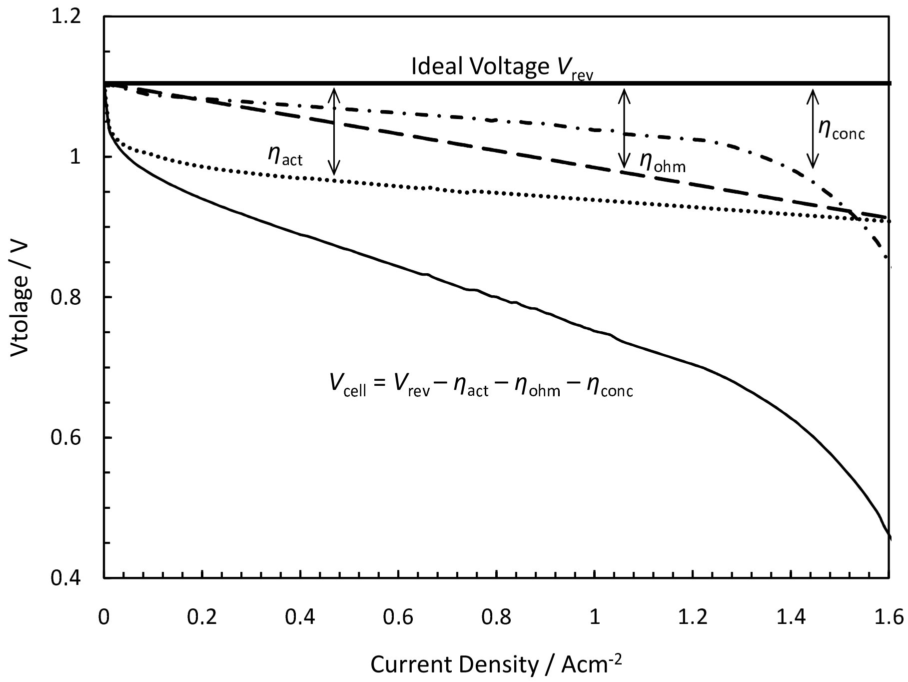

Figure 1.2: *V*-*i* curve showing how losses due to η_{act}, η_{ohm}, and η_{conc} are combined to obtain the actual cell voltage.

The actual cell voltage V_{cell} is found by subtracting the overpotentials from the ideal voltage:

$$V_{cell} = V_{rev} - \eta_{act} - \eta_{ohm} - \eta_{conc} \tag{1.9}$$

The power produced by a fuel cell is equal to the product of voltage and current, as shown in Figure 1.3, which plots voltage and power density against current density. As more power is drawn from the cell, current increases and voltage decreases until peak power is reached.

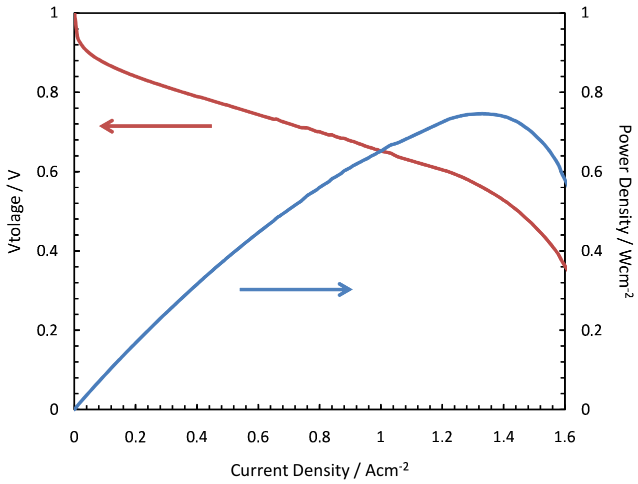

Figure 1.3: Cell voltage and power density versus current density, measured on a commercial PtRu MEA from BASF Fuel Cells. Anode fuel is H_2, cathode oxidant is air, both stoichiometric ratios are fixed at 2.2. Cell, anode, and cathode temperatures are at 70 °C and backpressure is 2 bar gauge on both sides.

1.1.2 Fuel Cell Components

The heart of a fuel cell is the membrane electrode assembly, or MEA, which consists of an anode and a cathode on either side of an ion-conducting membrane. In the case of low-temperature PEM fuel cells, the membrane is usually a proton-conducting perfluorosulfonic ionomer, commonly known by the trade name Nafion. Since protons are transported through the membrane as H_3O^+ ions, for maximum conductivity the membrane must be fully saturated with H_2O. Water management and membrane hydration are important issues in PEMFC system design, as operating temperatures are generally capped at 90 °C for Nafion-based MEAs, thus the "low-temperature" designation.

Each electrode consists of a gas diffusion layer (GDL) and a catalyst layer

(CL). The GDL is a porous, electrically conducting material that allows easy gas transfer to the catalyst layer while conducting electrons out from the MEA. Common materials include carbon paper and carbon cloths. GDLs are sometimes treated with Teflon or another hydrophobic substance to improve water drainage from the MEA and decrease flooding, which could hinder gas transport. Microporous layers (MPL), often composed of carbon powder mixed with Teflon, can also be applied to the side of the GDL facing the catalyst layer to provide a flatter surface and improve contact between the two.

Figure 1.4 illustrates an electrode with a catalyst layer and MPL between a GDL and the ionomer membrane. The catalyst layer contains the catalyst nanoparticles, which are supported on a high surface area carbon substrate to provide electrical contact, and mixed with an ionomer to allow protons to flow to the membrane. The carbon particles of the MPL infiltrate into both the catalyst layer and GDL to to facilitate electric conductivity. Additionally, the catalyst layer must be sufficiently porous for reactants to reach the catalyst and for products to be removed. The electrochemically active surface area (ECSA) of a catalyst describes the surface area that is accessible to protons, electrons, and reactant gases — it can be significantly less than the catalyst's total surface area. The catalyst utilization, or ratio of ECSA to total surface area, is used to capture this discrepancy. Much research focuses on the optimum ratio of catalyst, carbon, ionomer, and other components in the catalyst layer to maximize utilization and transport.

An MEA is formed by applying catalyst layers to either to both sides of the membrane or to the anode and cathode GDLs, and then pressing the components

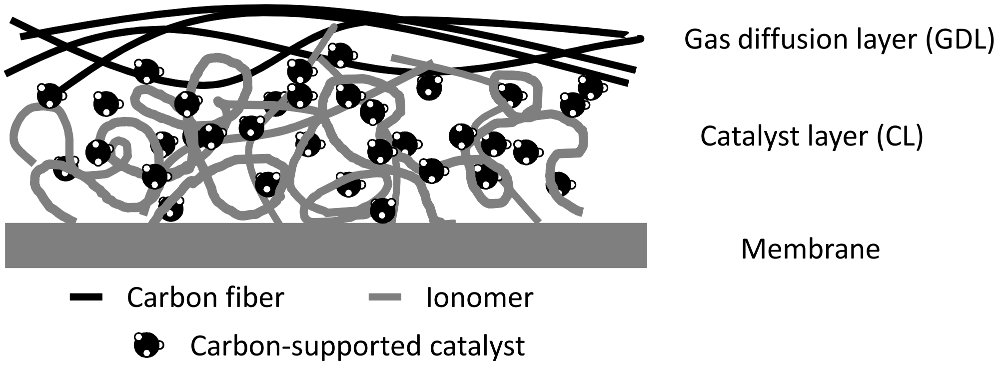

Figure 1.4: Illustration of a PEM fuel cell electrode (not to scale).

together. The anode and cathode catalyst layers can incorporate different catalysts and different catalyst loadings. During fuel cell operation the MEA is compressed between flow fields, which distribute reactants to the MEA and carry away unreacted gases and produced water. The flow fields are also conducting, and are connected to a current collecting plate. Heated and humidified flows are provided from an external test stand. MEAs must be sealed to prevent the anode and cathode gases from mixing; this can be accomplished in many ways including gaskets which compress around the anode and cathode. An MEA with gaskets and flow fields is shown in Figure 1.5. For practical use, MEAs are assembled into stacks and connected in series to increase the total voltage. In integrated PEMFC systems, components such as pumps and compressors, flow controllers, and heat exchangers are required to provide humidified flows and temperature regulation for the stack. These components are collectively known as the balance of plant (BOP).

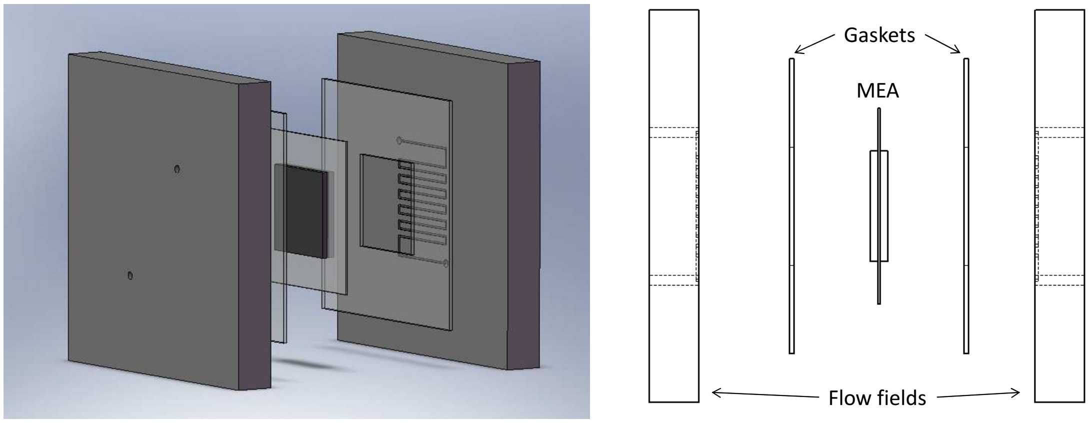

Figure 1.5: MEA with gaskets and flow fields.

1.2 CO Poisoning and Mitigation Strategies

The H_2 fuel for PEM fuel cells is most commonly produced by reforming hydrocarbons such as natural gas (methane) or gasoline, since such fuels are commonly available and are supported by existing distribution and storage infrastructure. Significant work is currently directed towards the development of PEM fuel cell systems integrated with reformers to allow direct operation from hydrocarbon fuels. Reforming breaks hydrocarbons into a mixture of H_2 and CO known as syngas. Two types of reforming are steam reforming and autothermal reforming (ATR). The general reforming reaction with steam to carbon ratio S/C and oxygen to carbon ratio O/C is 1.10

$$\mathrm{C}_n\mathrm{H}_m + n(S/C)\mathrm{H_2O} + \frac{n}{2}(O/C)\mathrm{O_2} \rightarrow \mathrm{H_2},\ \mathrm{CO},\ \mathrm{CO_2},\ \mathrm{H_2O},\ \mathrm{CH_4}. \tag{1.10}$$

To further increase the H_2 fraction, the reformate can then be passed into a water-gas-shift (WGS) reactor. The water-gas-shift reaction is:

$$\mathrm{CO} + \mathrm{H_2O} \rightarrow \mathrm{CO_2} + \mathrm{H_2}. \tag{1.11}$$

For an ATR reactor, which will be employed in the system modeling section of this study, WGS effluents are typically in the range of 30–40% H_2, 2–20% H_2O, 5–10% CO_2, and 2–10% CO, along with residual hydrocarbons (<1.0% total on a wet basis [1]).

It is not feasible to use WGS effluent from an ATR or steam reformer as the anode feed in a PEM fuel cell with pure Pt catalysts since Pt is severely poisoned by even parts-per-million (ppm) levels of CO at typical PEM fuel cell operating conditions (below 100 °C). The strong affinity of CO for Pt and the inability for O to oxidize Pt-CO adsorbates at such low temperatures causes a layer of CO to block active sites from being used in H_2 oxidation and reducing power output to inoperable levels. Reducing the poisoning effects of CO on anode electrocatalysts for low-temperature, Nafion-based PEM fuel cells (PEMFCs) is essential for the commercial viability of PEMFC systems operating with hydrocarbon fuel reformers.

Two approaches to the CO-poisoning problem are discussed in this study: the development of reformate tolerant anode electrocatalysts, and more complete purification of the reformate to remove CO. Other techniques include air bleeds and voltage pulsing or periodic short-circuiting of the cell to aid *in-situ* CO oxidation. However these approaches degrade efficiency as well as catalyst lifetime [2]. High-temperature (120 °C–160 °C) PEM fuel cell operation is also an option, as CO oxidation penalties decrease with rising cell temperatures, but high-temperature operation with Nafion membranes is extremely difficult because Nafion must be kept fully humidified to achieve good proton (H_3O^+) transport [3]. Alternative membranes such as polybenzimidazole (PBI) based materials are gaining commercial success, but such systems have relatively poor power densities and durabilities in comparison to more mature Nafion-based systems [4]. Successful implementation of CO tolerance will most likely derive from a combination of mitigation strategies.

1.2.1 CO Tolerant Anode Electrocatalysts

The high performance of PEM fuel cells utilizing pure Pt catalysts is substantially decreased by even tiny amounts of CO in the anode feed. Early studies showed that the maximum power density obtained from a Pt PEM fuel cell was halved by the introduction of 5 ppm CO [5]. Nonetheless, alternative non-Pt catalysts have not been able to match the extremely high H_2 oxidation activity of Pt. Significant efforts have thus been made to develop Pt-based catalysts that retain high HOR activity even in CO concentrations up to 1–2%.

A wide variety of multi-metallic Pt alloys and mixtures have been investigated for CO tolerance. The most common catalyst for reformate-tolerance is a 1:1 PtRu alloy, which is available commercially and is currently being used in reformate-feed stacks. However, the use of PtRu catalysts for anodes still only permits less than 100 ppm CO in the anode inlet [6, 7, 8]. PtRu catalysts can tolerate slightly higher CO concentrations with lower anode overpotentials by employing mitigation strategies such as small air bleeds [9] or voltage pulsing [10, 11] for *in situ* CO removal. However, such mitigation strategies also have negative impacts on system efficiencies and architecture. Other binary catalysts that have been tested include PtMo [6, 12, 13], PtSn [14, 15, 16], PtW [12]. Additional studies focus on ternary or even quaternary Pt-based mixtures. These multi-metallic catalysts are generally believed to increase CO tolerance by the bi-functional mechanism, in which electronic effects reduce the surface affinity for CO, while the alloying element also binds an oxygen species and facilitates CO oxidation.

Of these catalysts, various configurations of Pt-Mo have drawn attention in recent years. Numerous studies have shown enhanced CO tolerance of PtMo alloys [17, 6, 13] and Pt/MoO$_x$ heterogeneous catalyst [18] over PtRu catalysts. Notably, Mukerjee et al. demonstrated a threefold increase in CO tolerance over PtRu catalysts in 100 ppm CO, using a PtMo alloy [6]. However, there is a wide range of performance reported in the literature due to the numerous synthesis routes employed and the resulting variation in composition and structure. Some studies report inferior CO tolerance of Pt-Mo catalysts compared to PtRu, and the durability of Pt-Mo catalysts is also in question. The situation is complicated by the frequent lack of detailed characterization confirming the catalyst architecture.

It is widely reported that Pt-Mo catalysts exhibit a decrease in activity as shown by thin-film cyclic voltammetry, over potential cycling between 0.1 and 0.5 and up to 0.8 V [19, 20, 21]. Lebedeva performed cycling on an MEA with PtMo anode and Pt cathode, and after cycling discovered signature Mo peaks on the cathode, clearly showing Mo dissolution into the acidic electrolyte and migration across the membrane [19]. This leaching lowers the Mo content in the catalyst and reduces the catalyst activity of the anode. Additionally, metal leaching can cause dehydration of the Nafion membrane, reducing its proton conductivity, and increase cathode polarization. Loss of Mo from PtMo catalysts is attributed to high oxidation states of Mo at anode potentials greater then 0.2 V, which create MoO_3 species which are soluble in the acidic Nafion environment [22].

Recent studies have demonstrated that Mo oxidation and loss are decreased in more homogeneous and crystalline PtMo alloy catalysts compared to amorphous mixtures [19, 23]. This provides additional motivation for efforts to improve the durability and performance of bimetallic catalysts in PEMFCs by taking advantage of well-controlled electrochemical or liquid-phase synthesis techniques which can provide structures such as core-shell nanoparticles with only durable Pt on the outer catalyst particle surfaces [24, 25]. Density functional theory (DFT) studies suggest that such core-shell architectures with Pt shells on various metals and metal alloys may provide enhanced activity for CO oxidation [26, 27] and further provide improved durability of the base metal-containing catalysts with the Pt shell. Preliminary investigations of well-defined $Pt_{0.8}Mo_{0.2}$ alloy and MoO_x@Pt core-shell (Mo core, Pt shell) electrocatalysts have indeed demonstrated a significant improvement in CO tolerance compared to PtRu catalysts [25].

1.2.2 Reformate Purification and Cleanup

Fuel-side cleanup and removal of CO from the reformate stream is another area of research for PEMFC systems. Currently most hydrocarbon reformers are linked to low-temperature PEM fuel cells through some form of H_2 purification process, which complicates the PEMFC system at the expense of economic viability, system weight and size, and overall system efficiency. The flow diagram in Figure 1.6 illustrates the complex interactions between the numerous components required to operate a PEM fuel cell system on a hydrocarbon fuel. This system integrates the PEM fuel cell stack with a liquid fuel processor including an autothermal reformer, WGS reactor, and a preferential CO oxidation (PROx) reactor for partial CO removal.

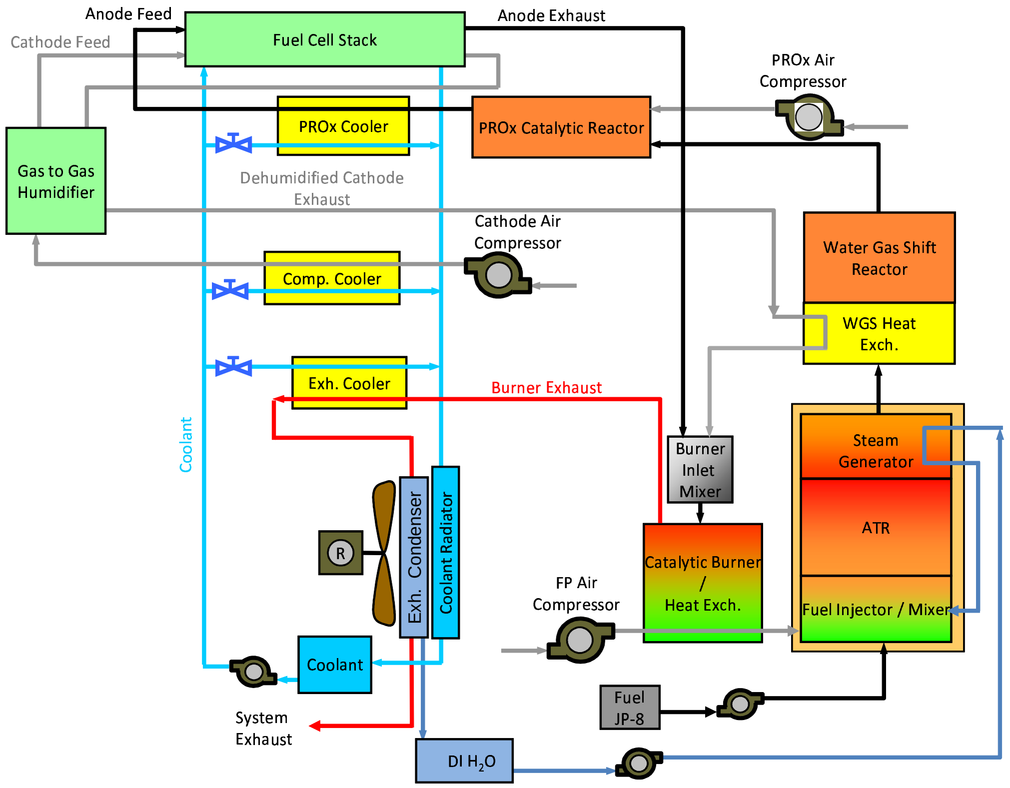

Figure 1.6: Flow diagram showing schematic of a hydrocarbon-fueled PEM fuel cell system with fuel processor, PROx reactor, catalytic exhaust burner, liquid-cooled fuel cell stack, exhaust condenser for water recovery, and balance of plant components.

In addition to PROx reactors [28, 29], other methods for H_2 purification include pressure-swing absorption (PSA) reactors [30] and Pd-based membrane purifiers [31, 32]. These approaches provide near-complete CO elimination, whereas the PROx reactor only provides partial cleanup down to 10–100 ppm CO. However, the PROx system avoids the penalties of including two large reactors and the regeneration process associated with PSA, and the increased parasitic loads associated with high-pressure reformer operation required by Pd-based membranes.

The PROx reaction is

$$2CO + O_2 \rightarrow 2CO_2. \tag{1.12}$$

Oxygen (or air) is introduced to the reformate in the presence of a catalyst which preferentially oxidizes CO, rather than performing parasitic H_2 oxidation,

$$2H_2 + O_2 \rightarrow H_2O. \tag{1.13}$$

Two parameters characterize the performance of PROx reactors — CO selectivity and CO conversion. CO selectivity is the percentage of O_2 that is consumed for CO oxidation. Higher CO selectivities are preferred in order to decrease CO concentrations and avoid loss of H_2. CO conversion is simply the percentage of CO entering the reactor that is oxidized to CO_2. These two parameters are affected by the choice of PROx catalyst, and temperature and size of the reactor. Reactions 1.12 and 1.13 are highly exothermic, and also must be kept in a tight temperature range to maintain high CO selectivity; this encourages a modular design where a multi-stage PROx reactor is employed with cooling at each stage. Such configurations are used to achieve the high conversion rates necessary to reduce CO concentrations to ∼10 ppm. PROx systems thus offer flexibility in that as anode electrocatalysts are developed with improved CO tolerance, the PROx demands may be reduced, allowing smaller, cheaper reactors to be used.

1.3 Modeling PEM Fuel Cell Systems with Fuel Processing and CO Cleanup

Current CO cleanup strategies for linking conventional low-temperature PEM fuel cell stacks with hydrocarbon reformers greatly increase the overall system size and complexity because of high temperatures in the fuel processor and the need for heat exchangers and reactors to cool the reformate, clean-up and burn the CO in the reformate, and capture the necessary water for running the reformer. System-level models are a valuable design tool used to analyze such systems, an example of which is shown in figure 1.6, utilizing a PROx reactor for CO cleanup. Modeling the hydrocarbon fuel processing, PROx reactor CO clean-up, PEM fuel cell stack, and the balance of plant presents significant challenges because of the complex thermal integration and mass flow recycling for recovering water in the system. Balance of plant components including air compressors/blowers, liquid pumps, and a radiator fan present parasitic loads to the system that will vary strongly with operating conditions, power loads, and individual component performance. For the high level analysis, integrated system models with lumped analysis for individual components [32, 33, 34, 35, 36, 37] provide an effective means for evaluating system design and performance of complex integrated PEM fuel cell power plants with hydrocarbon fuel processors. These studies have been conducted with various fuel reforming and CO removal systems. However to date, system models have not clearly examined the impacts of CO and CO tolerant stacks on system performance. Past studies with PROx reactors in the system have often assumed that the PROx is 100% effective or that the CO is reduced to sufficiently low concentrations entering the fuel cell stack that performance is unaffected [35].

Recent advances in anode electrocatalyst design suggest that with a new generation of CO tolerant electrocatalysts, the reduced losses in current density due to CO at typical operating voltages may allow for reduced reformate clean-up and simplify a PEM fuel cell system with hydrocarbon fuel processing for H_2 production. In general, the increased tolerance for CO in PEM fuel cell anodes reduces the need for H_2 purification and thereby the penalties in overall efficiency resulting from fuel processing and purification in hydrocarbon-fueled PEM fuel cell systems. There is additional value in studying the specific system and component-level impacts of improved CO tolerance.

1.4 Goals and Objectives

This work investigates two aspects of CO tolerance in PEM fuel cell systems: 1) experimental characterization of the CO tolerance of MEAs fabricated with two promising Pt-Mo catalysts, and 2) utilizing system-level modeling to explore the implications of CO tolerance on PEM system performance and design.

Fundamental studies of $Pt_{0.8}Mo_{0.2}$ and MoO_x@Pt core-shell catalysts using thin-film electrodes in liquid electrolyte indicate a significant increase in CO tolerance of the PtMo alloy over a commercial PtRu catalyst, and that the MoO_x@Pt catalyst's performance surpasses even the PtMo [25]. This study seeks to demonstrate the same CO tolerance from the two catalysts in MEA configuration. Differences in catalyst and Nafion loadings between thin-film and MEA electrodes, as well as the shift from liquid to gas-phase reactants, may result in significantly different performance. The durability of Mo-containing catalysts in MEA environments is also uncertain. Thus, stability testing will also be performed to address this issue. It is hoped that the core-shell architecture will afford some protection to the MoO_x core and result in reduced Mo loss due to leaching.

Because variations in materials, fabrication methods, and testing conditions complicate comparisons between published studies, performance benchmarks are incorporated into the study. In-house MEA fabrication methods are validated by comparing MEAs incorporating a commercial PtRu catalyst to complete MEAs that were purchased. The same in-house fabricated PtRu MEAs are used to provide a baseline of CO tolerance to judge the Pt-Mo MEAs against.

Additionally, a system-level model is used to analyze a PEM fuel cell generator with an integrated fuel processor and PROx reactor, operating on liquid hydrocarbon fuel. The model enables an assessment of potential gains in system performance that may be realized with advances in stack CO tolerance. Specifically, an increase in the tolerable CO concentration in the anode feed could allow for reduced PROx reactor CO selectivities and CO conversions and corresponding benefits to system complexity, size, and cost.

This study aims to accomplish the following:

- establish standard fabrication and testing protocols for GDEs and MEAs utilizing various anode electrocatalysts resulting in reproducible MEA performance

- characterize the V-i performance and stability of PtMo and MoO_x@Pt electrocatalysts in pure H_2 and CO contaminated streams, and compare to a PtRu benchmark

- evaluate the impacts of anode CO tolerance on the performance of a PEM fuel cell generator integrated with a liquid hydrocarbon fuel processor and PROx reactor for CO cleanup, specifically examining system efficiency, balance-of-plant components, and PROx reactor conditions

Chapter 2 provides the experimental methods used for fabrication and testing of MEAs and discusses challenges encountered while developing the fabrication procedures. Chapter 3 presents results of the MEA testing and compares the CO tolerance and stability of the PtMo and MoO_x@Pt catalysts. Chapter 4 describes the system-level model of a PEM fuel cell system and positive impacts of CO tolerance of system performance. Conclusions and recommendations for future work are discussed in Chapter 5.

Chapter 2

Experimental Methods for MEA Fabrication and Testing

Single-cell MEA tests were carried out to characterize the fuel cell performance of the PtMo and MoO_x@Pt catalysts synthesized at the University of Maryland and previously characterized by thin-film rotating-disk electrode studies. Since comparable MEAs had not previously been fabricated at the University of Maryland, two types of benchmarks were employed to validate the basic level of MEA performance. Commercial PtRu MEAs with limited reformate-tolerance were purchased, as were the individual components comprising the commercial MEA. This enabled a comparison between the commercial MEAs and MEAs fabricated in-house with identical components, and also between MEAs containing the new catalysts and those made with the conventional PtRu catalyst. Fabrication methods were not perfected to fully optimize MEA performance, but rather methods were developed to obtain consistent performance with relatively high power densities for viable electrocatalyst layers. The cathode and membrane materials were held fixed using the commercial supplies and only the anode catalyst layer was varied with the different formulations, allowing direct comparison of the catalyst performance. All MEAs were tested on the same equipment under the same conditions, and representative samples were also analyzed before and after testing.

2.1 Nano-architectured Catalysts

2.1.1 Synthesis

PtMo alloy and MoO_x@Pt core-shell nanoparticles were prepared in-house by methods previously described by Liu et al. [25] and briefly reviewed here.

Solution-based syntheses of PtMo alloy nanoparticles are challenging due to the large negative redox potential of the Mo^{n+}/Mo^0 couple and the low miscibility of Pt and Mo. For this synthesis, co-reduction of $MoCl_3$ and $Pt(acac)_2$ in phenyl ether was used with sodium triethylborohydride and oleic acid as the reducing agent and capping agent, respectively. The PtMo was heat-treated post-synthesis in a reducing environment to remove the oleic acid before supporting the nanoparticles on a carbon support.

For the MoO_x@Pt core-shell synthesis, $NaBH_4$ reduction of $MoCl_3$ in ethylene glycol was employed in conjunction with the weakly-coordinating polyvinylpyrrolidone (PVP) stabilizer to form MoO_x nanoparticles. These particles were then reacted with $PtCl_2$ in ethylene glycol to give MoO_x@Pt core-shell nanoparticles with 1~2 layers of Pt atoms forming shells over MoO_x cores [25]. The PVP stabilizer near the catalyst surface was not removed from the core-shell particles by heat treatment due to concerns about high-temperature particle restructuring. From thermogravimetric analysis (TGA) of the carbon-supported core-shell catalyst it was estimated that PVP added an additional ~40% to the metal weight.

2.1.2 Characterization

X-ray diffraction (XRD), transmission electron microscopy (TEM), energy dispersive X-ray analysis (EDX), extended X-ray adsorption fine structure (EXAFS), and X-ray photoelectron spectroscopy (XPS) were used to verify the size, composition, and nano-architecture of the nanoparticles [25]. The PtMo alloy nanoparticles were found to be 3 nm across, and composed of 80% Pt to 20% Mo (atom %). The MoO_x@Pt particles were slightly larger at 3.5 nm, and were 40% Pt and 60% Mo (atom %).

Thin-film rotating disk electrode (RDE) and cyclic voltammetry (CV) experiments were performed to characterize the electrochemical performance of the catalysts. H_2SO_4 was used as a liquid electrolyte, and neat and CO-contaminated H_2 were bubbled in to saturate the solution for CV and RDE experiments. Figure 2.1 shows diagrams of the alloy and core-shell nanoparticles, as well as CV and RDE data comparing their performance in pure H_2 and 1000 ppm CO, respectively. In both cases MoO_x@Pt shows superior performance, suggesting that the residual PVP does not negatively impact catalyst performance in the liquid solution experiments. However, as discussed later, it remains unclear what the impacts of the stabilizer are on the Nafion/catalyst interface in MEAs and its impact on electrocatalyst layer effectiveness. Further details on the methods and results of catalyst characterization can be found in [25] and its supporting information.

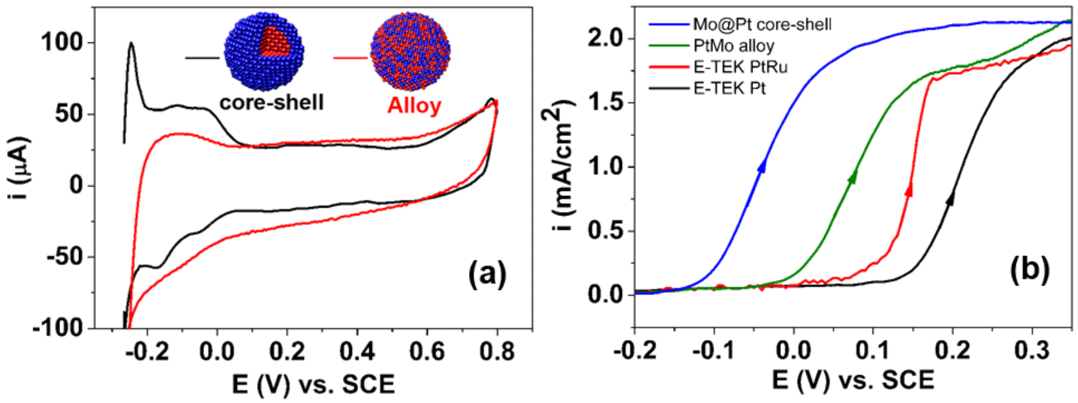

Figure 2.1: (a) Cyclic voltammograms of PtMo alloy and MoO_x@Pt core-shell catalysts in 0.5 M H_2SO_4 at 25 °C, scan rate 100 mVs^{-1}. (b) RDE polarization for H_2 oxidation in 1000 ppm CO on different catalysts (all 30% metal loading on carbon XC-72) at 25 °C, rotation 1600 rpm, scan rate 1 mVs^{-1}.

2.2 MEA Fabrication

A literature survey was conducted to provide guidance in designing the MEA fabrication process, and is summarized in Table 2.1. Fabrication methods can be broadly categorized according to how the catalyst layer is formed. Catalyst-coated membrane (CCM) methods involve direct or indirect (through a decal transfer) application of the catalyst layer to the Nafion membrane, and then assembly with the anode and cathode GDLs. Another increasingly common method is to create gas diffusion electrodes (GDEs) by applying the catalyst layer onto the GDLs before hot-pressing with the membrane. Ink may be transfered onto the membrane, decal, or GDL in many ways, such as casting, brushing, screen printing, spraying, or sputtering. In either case, a variety of solvents are used to prepare catalyst inks, and there is a wide range of final catalyst and Nafion loadings found in the catalyst layers.

Forming GDEs by brushing catalyst ink onto a GDL was selected as the fabrication method for this work due to the relative simplicity in the number of ingredients and fabrication steps. Even so, due to the relatively few publications that listed specific ink ingredients and even fewer that provided exact ratios and mixing methods, much trial and error was required to develop inks which led to adequate MEA performance, as discussed below.

Table 2.1: Summary of literature regarding catalyst ink and MEA fabrication methods. x indicates that an ingredient was used but no quantity was given, and ? indicates that no information was provided.

Ink application method		Loading / wt %			Ink composition			Hot-press conditions			Reference
		Catalyst	MEA		wt ratio, catalyst/C is 1			Temp.	Pres.	Time	
		Metal/C	Catalyst	Nafion	IPA	Water	Other	/ °C	/ MPa	/ min.	
CCM	cast/decal	20-30	21	29			Glycerol, TBAOH	x	x	x	[38, 39]
CCM	brush/decal	20	14	30		x					[40]
GDE	spray	20	13	38	5-8	20-32		130	4.9	1	[41]
GDE	brush/roll	20	16	20	x			130	6.9	1	[42]
GDE	screen print	60	42	30		x		125	10	1.5	[43]
GDE	print/paint	10	7	33	5% Nafion solution only			155	6.9	2	[44]
GDE	brush	20	14	29	15 parts IPA + H_2O			120	49	2	[22]
GDE	brush/roll	30	26	13	?	?	?	140	98	3	[17, 6]
GDE	brush	30	19	38	31	20		140	8.8	2	This study

2.2.1 Materials

50 μm thick Nafion 212 membrane (Ion Power Inc, New Castle, DE) was cut into 4 cm x 4 cm squares and treated to remove impurities and convert to H^+ form prior to hot-pressing. Treatment consisted of 1 hour in lightly boiling 3% H_2O_2, 2 hours in lightly boiling water, then 1 hour in lightly boiling 0.5 M H_2SO_4 [45, 46, 47]. Membranes were then rinsed three times in lightly boiling water and stored in de-ioinized water. Before use, membranes were dried overnight in air in a covered petri dish at room temperature.

Woven carbon cloth cathode GDEs with 0.5 mg·cm^{-2} Pt/C (30 wt%) and a hydrophobic microporous layer were puchased from BASF Fuel Cell (Somerset, NJ), as was 30 wt% 1:1 PtRu/C alloy catalyst powder supported on XC-72 carbon black.Plain GDL with a non-Teflon-treated microporous layer was also obtained from BASF Fuel Cell for fabricating the anodes. 200 μm perfluoroalkoxy (PFA) gasket material was obtained from BASF Fuel Cell (Germany) and cut into 6 cm x 6 cm squares. 5% Nafion solution (1100 EW) in alcohols, isopropyl alcohol, peroxide and sulfuric acid were purchased from Sigma Aldrich (St. Louis, Missouri) and used as received. Fiberglass-reinforced teflon tape (FRT) for use in hot-pressing was donated by Precision Coating (Dedham, MA). Complete 5 cm^2 MEAs (series 12W) with 0.5 mg·cm^{-2} PtRu (1:1) anodes were also purchased from BASF Fuel Cell in order to provide benchmark performance for the MEAs fabricated in this study. The membrane and cathode GDEs of the purchased MEAs were identical to those used to fabricate in-house MEAs.

2.2.2 Catalyst Ink

Catalyst ink was prepared by first creating a stock solution of 5% nafion solution, isopropyl alcohol, and in some cases water. The stock was sonicated in a water bath for 1 hour to thoroughly mix the components, then quickly pipetted over the catalyst to prevent burning during the exothermic reaction between the carbon and alcohols. PtRu and PtMo catalyst inks were prepared using a carbon-supported catalyst to 5% Nafion solution to IPA weight ratio of 1:12:31. For the MoO_x@Pt catalyst 20 parts water were also added to the ink. The ink was sonicated for 15–30 minutes; at this point inks of varying consistencies were obtained (examples are shown in Figure 2.2), but further sonication did not result in noticeable improvement and over-sonication has been shown to reduce catalyst active surface area [48] . Water in the sonication bath was changed frequently to protect the catalyts from degredation due to high temperatures. Throughout the fabrication process the ink was mixed continuously with a micro stir bar, and sonicated for 20–30 seconds immediately before brushing each layer. A minimum of 20 mg of catalyst powder was required to prepare a single 5 cm^2 MEA with 0.5 $mg\cdot cm^{-2}$ metal loading, since over half of the ink solids were lost to the brush and vial walls. It may be possible to reduce these losses by using a smaller brush and vial.

Two main problems were encountered when making catalyst inks: particle agglomerates, and the consistency and stability of the ink. The former is influenced by the choice of solvents as well as the catalyst synthesis process and resulting surface properties, and impacts the structure of the catalyst layer and catalyst utilization. The latter affects the composition of the catalyst layer (for example, if a large chunk of carbon-supported catalyst does not become wetted and dispersed, the catalyst:Nafion ratio in the remainder of the ink will be changed), and is also a concern in terms of uniformity through the catalyst layer and repeatability between MEAs.

A mixture of catalyst powder, 5% nafion solution, and isopropyl alcohol (IPA) was used for the BASF PtRu catalyst ink, which produced a smooth dispersion when sonicated, with no particles in the solution visible to the eye, as shown on the left in Figure 2.2. However when preparing inks with the PtMo alloy, the same ink recipe yielded a very granular suspension regardless of sonication time (right, Figure 2.2). Both inks also contained unwetted clumps of catalyst that remained even after sonication. Clumps were <1 mm diameter in the PtRu ink, but up to 2 mm diameter in the PtMo ink. Additional IPA and water were used to dilute the PtMo ink and modify the dieletric constant of the solvent solution in hopes of reducing agglomerates and producing a finer suspension, but none of the resulting solutions were stable over more than a minute. During sonication the ink consistency approached the uniform texture of the PtRu ink but particles agglomerated and settled out within minutes after the vial was removed from the sonication bath. MoO_x@Pt inks including water achieved the smooth consistency of the PtRu ink shown in Figure 2.2. To prevent settling, ink was mixed continuously with a magnetic stir bar and also sonicated briefly before each layer was brushed. MEAs were fabricated with three different catalyst ink recipes, and the best results, obtained from Nafion/IPA inks for PtRu and PtMo and Nafion/IPA/water for MoO_x@Pt, are presented in the following chapter.

Figure 2.2: BASF PtRu (left) and PtMo (right) catalyst inks prepared with a 1:12:31 catalyst:Nafion solution:IPA weight ratio.

Other methods of preparing catalyst inks were also investigated. A Branson probe sonicator with 1/8” tip was used to mix catalyst ink solutions in hopes that the higher power would be successful in breaking up unwetted clumps of catalyst remaining from the heat treatment process. Catalyst powders were mixed with Nafion, IPA, and water in plastic 15 mL tubes and placed in a ice bath to prevent boiling of the liquid during sonication. The probe was submerged in the ink mixture and operated at a 50% duty cycle for up to 10 minutes, but chunks were still observed and the resulting suspensions were unstable and catlayst settled out of solution almost immediately.

Ball-milling was also attempted as a way to break up chunks. A thick slurry of catalyst, Nafion, and IPA was mixed in a small 10 mL glass vial together with fifteen 5 mm diameter zirconia balls, then ball-milled for one hour. Almost all chunks were successfully ground down, however particles were still visible in the PtMo ink (see Figure 2.3) and recovery of the catalyst ink was difficult due to the small volumes used. Additionally, as observed elsewhere [48] TEM of ball-milled ink showed significant detachment of PtRu nanoparticles from the carbon support compared to inks prepared by other methods, so this method was not further pursued.

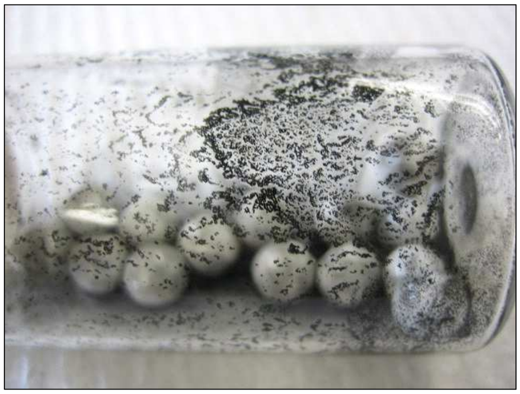

Figure 2.3: PtMo catalyst ink prepared with 5% Nafion solution and IPA after 1 hours of ball-milling.

Attempts to form a more viscous ink for screen-printing were unsuccessful because the catalyst powder would not disperse evenly in smaller amounts of solvents. Methods such as high shear mixers [49] and homogenizers [19] have been utilized to produce well-dispersed, highly stable catalyst inks. However this equipment was unavailable.

2.2.3 GDE and MEA

The anode catalyst layer was formed by brushing the catalyst ink onto a carbon-cloth GDL using a paint brush (5/16” width, from McMaster-Carr). The GDL was rotated 90° after each coat to evenly distribute the catalyst, and dried at 60 °C between successive layers. After drying the electrode was weighed to determine how much material was added; depending on the ink 10–20 layers were required to reach the total metal loading of 0.5 $\text{mg}\cdot\text{cm}^{-2}$. After the desired loading was obtained, the completed anode GDE was fully dried in the 60 °C oven for at least one hour.

It was assumed that the catalyst layer composition matched that of the ink, so that the final PtRu and PtMo layers consisted of 2.5 mg of metal on 5.8 mg of carbon, with 5.0 mg of Nafion. The MoO_x@Pt catalyst layer also contained an additional 1 mg of PVP attached to the catalyst nanoparticles (estimated from the TGA metal:PVP ratio). Due to agglomeration as previously discussed or preferential loss of one phase (for example Nafion, but not catalyst, sticking to the brush), the actual catalyst layer composition could be significantly different than expected. Elemental analysis techniques such as inductively coupled plasma mass spectrometry (ICP-MS) or neutron activation analysis (NAA), could be used to better quantify the actual catalyst and Nafion loadings in the MEA.

To form the MEA, the anode and cathode GDEs were aligned on either side of a dry Nafion square, between two sheets of fiberglass-reinforced Teflon, to reduce sticking. The MEA and FRT were clamped between two flat aluminum plates and inserted into the hot press, which was preheated to 140 °C. The plates were allowed to warm up for 5 minutes without compression, then the MEA was pressed for 2 minutes at 8.8 MPa. After pressing, the MEA was removed from the press and allowed to cool on the bench top at room temperature for at least two hours before removing it from the aluminum plates and FRT.

2.3 MEA Testing

2.3.1 Experimental Setup

PFA gaskets were cut to snugly fit around each GDL while extending past the edges of the Nafion membrane, so that when compressed they formed a tight seal around the MEA edges. The MEA with a gasket on each side was aligned in a 5 cm^2 test fixture with serpentine channels in graphite flow fields from Fuel Cell Technologies (Los Alamos, NM), similar to the assembly of Figure 1.5. Greased (Krytox, McMaster-Carr) bolts were tightened to 12.5 N·m of torque with a torque wrench to compress the MEA and gaskets. The test fixture was located inside of a fume hood and exhaust was also vented inside the hood to contain the excess H_2 and CO. A Scribner Associates (Southern Pines, NC) 850e test stand was used to provide mixed and humidified flows, backpressure, and to control the cell voltage or current. An Autolab PGSTAT30 potentiostat and 10 A current booster (Eco Chemie, Netherlands) were used for frequency response analysis and cyclic voltammetry. Pure H_2 and H_2/CO mixtures up to 1000 ppm were used as anode feeds, while air was the cathode oxidant. CO mixtures at 100 and 1000 ppm were obtained and diluted using mass flow controllers. Filtered air was supplied from an in-house compressor. All other gases were from Airgas (Allentown, PA).

2.3.2 Procedures

The cell was operated at 70 °C, with 2.0 bar gauge backpressure on both sides. Both cathode and anode flows were humidified to saturation at the same temperature as the cell. Flow stoichiometry, the ratio of reactant supplied to reactant consumed, was set at 2.2 on both sides of the MEA, with minimum flow rates of 56 and 133 sccm on the anode and cathode, respectively, to facilitate water removal. Operating conditions are summarized in Table 2.2.

Table 2.2: MEA parameters and operating conditions.

Condition	**Value**
MEA parameters:	
Cell geometric area / cm^2	5
Anode catalyst	PtRu, PtMo, or MoO_x@Pt
Cathode catalyst	Pt
Anode catalyst (metal) loading / $mg \cdot cm^{-2}$	0.5
Cathode catalyst (metal) loading / $mg \cdot cm^{-2}$	0.5
MEA operating conditions:	
Cell temperature / °C	70
Anode humidifier temperature / °C	70
Cathode humidifier temperature / °C	70
Anode fuel	H_2 with 0–1000 ppm CO
Cathode oxidant	Air
Stoichiometric ratio of anode H_2 flow	2.2
Minimum anode H_2 flow rate / sccm	56
Stoichiometric ratio of cathode air flow	2.2
Minimum cathode air flow rate / sccm	133
Anode backpressure / bar (gauge)	2
Cathode backpressure / bar (gauge)	2

MEAs were conditioned overnight at a constant 0.6 V before testing. CO-contaminated H_2 was then introduced and the cell was poisoned for 1.5–2.5 hours while maintaining 0.6 V, until a constant current density was reached. V-i curves were recorded after equilibrium was reached, at intervals of 50 and 10 $\text{mA}\cdot\text{cm}^{-2}$ after 20 seconds at each point to stabilize. Measurements were halted after cell voltage dropped below 0.5 or 0.45 V to avoid damage to the catalysts. Ohmic resistance of the cell was measured by the current-interrupt method at each point. CO concentrations of 25, 50, 100, 250, 500, and 1000 ppm in H_2 were tested sequentially. The cell was then recovered for 12–18 hours in pure H_2 before repeating the CO sequence. CO testing was performed 2–3 times for each MEA. For stability testing the cell was held at 0.6 V in 100 ppm CO for 1–5 additional days following the recording of V-i curves. At least two MEAs incorporating each catalyst were tested.

Electrochemical impedance spectroscopy (EIS) and CV were also performed, using the frequency response analyzer built into the Scribner as well as the Autolab system. For the EIS, galvanostatic control was used,frequencies were swept between 10 kHz and 0.1 Hz, and excitation amplitudes were kept to 10% of the steady state signal or 10 mA. For CV measurements, both anode and cathode were purged with nitrogen for 30 minutes to an hour before the cathode was switched to H_2 and the anode flow rate was reduced to a few sccm. Voltage was swept from 0 to 0.8 V at 20 mVs^{-1}, using the cathode as a hydrogen reference. For CO-stripping, 100 ppm of CO in H_2 was flowed over the anode for 30 minutes to poison the anode, followed by 1 hour of N_2 to purge the hydrogen before scanning the voltage from 0 to 0.8 V.

2.4 Physical Characterization

MEA cross-sections were visualized before and after testing using a Hitachi S70 scanning electron microscope (SEM). SEM-EDX was also used to visualize the elemental distribution through MEAs. MEA cross-sections for SEM were prepared by using a clean razor blade to slice through the MEA, with the cathode on top to minimize contamination from the anode.

For post-testing TEM analysis, catalyst material was scratched off from the anode catalyst layer of the MEAs and then dispersed in IPA. After a 5 minute sonication, 10 μL of the dispersion was cast on the TEM grids for analysis with a micropippet. TEM images and EDX of the catalysts were obtained on a JEM 2100 LaB6 TEM operating at 200 kV.

2.5 Fabrication Results

An representative SEM image of an in-house fabricated PtRu MEA cross-section is shown in Figure 2.4. The gas-diffusion layers (GDL), microporous layers (MPL), and catalyst layers (CL) of both anode and cathode are visible, sandwiching the Nafion membrane. Both catalyst layers can be distinguished from the microporous layer by their lighter color, as well as elemental composition as shown by EDX. There is some cracking in the catalyst layers and possibly a small gap between the anode and membrane. This separation most likely occurred when the MEA was cut to obtain the cross-section or while mounting for imaging, but in any case as adequate MEA performance was obtained and no macro-scale delamination

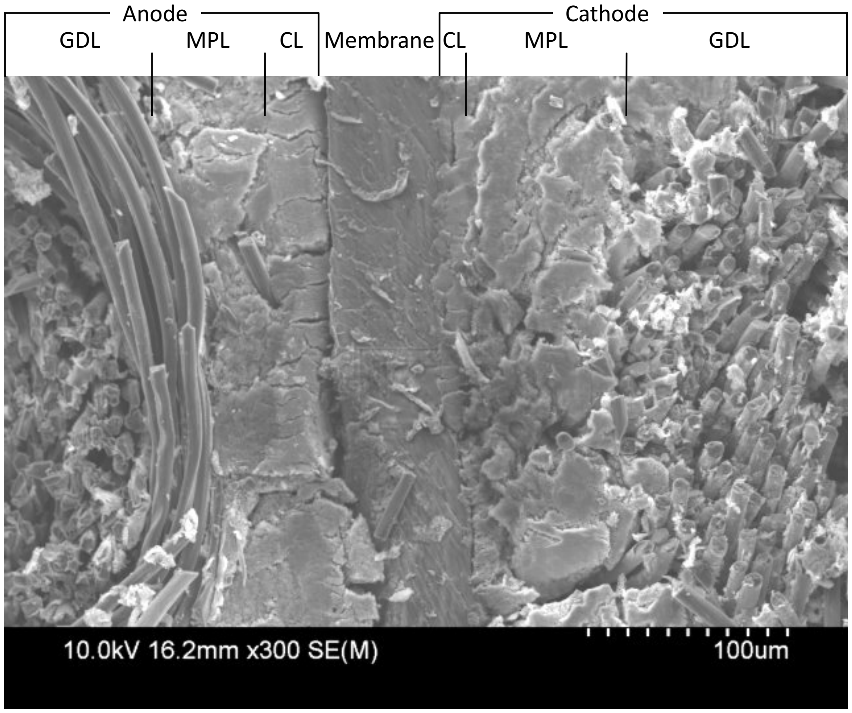

Figure 2.4: SEM image of an in-house fabricated MEA, showing anode and cathode gas diffusion layers (GDLs) with carbon fibers, microporous layers (MPLs), and catalyst layers (CLs) on either side of the Nafion membrane.

was observed, adhesion was not considered to be a problem. Anode catalyst layers that were created by brushing are generally ∼25 μm thick, while the commercial cathode catalyst layers are only 10–15 μm.

Figure 2.5 illustrates the overnight conditioning of a PtRu MEA, showing the initial increase in current density over time, then stabilization as the membrane becomes fully hydrated. Also shown is the testing cycle as the cell is held at 0.6 V for 2 hours, followed by two *V*-*i* curves at different scan rates, then returned to 0.6 V. Short (<2 second) drops in current density followed by a spike are caused by flooding of the gas channels of one of the flow fields momentarily starving the cell.

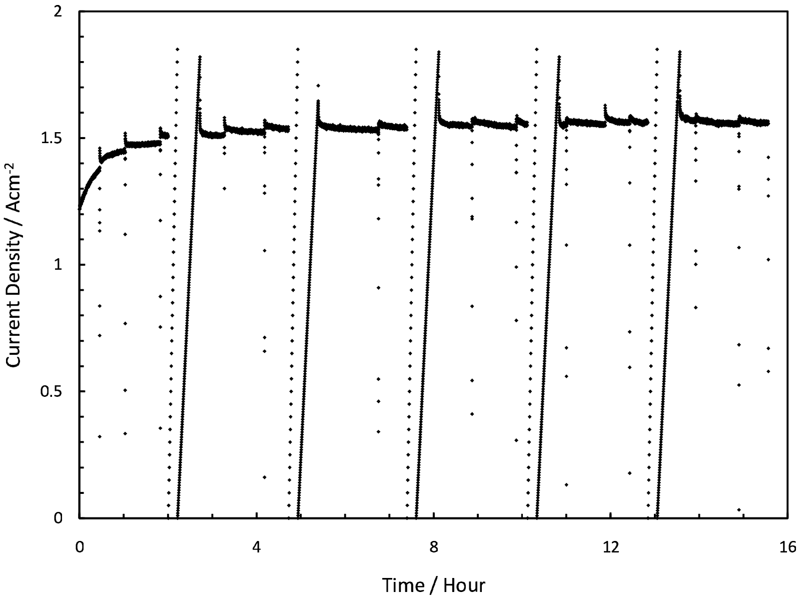

Figure 2.5: Current density increasing over time during overnight MEA conditioning. *V*-*i* curves are measured at two different intervals and scan rates every two hours.

After each cell was conditioned and its performance had stabilized, polarization curves were recorded at increasing CO concentrations. Figure 2.6 compares *V*-*i* curves of a commercial BASF MEA to an MEA fabricated in-house (designated as UMD) with identical cathode GDE, Nafion membrane, and anode GDL and PtRu catalyst. The current is normalized by the geometric area of the electrode, 5 cm^2 to produce the current density. Other metrics can be used to normalize the measured current, as will be discussed in Chapter 3. Curves are shown for pure H_2, and CO concentrations from 25 to 1000 ppm. Both MEAs were tested using the same procedures. The open circuit voltage (OCV) for this and all in-house fabricated MEAs is relatively low, between 0.91 and 0.95 V, compared to 0.97–1.0 V for the commercial MEA. This is likely due to leakage, i.e. reactant crossover.

Despite the low OCV, in general the performance of the two MEAs is comparable and consistent with PtRu MEAs in the literature. The UMD MEA exhibits superior H_2 performance at higher current densities. Both MEAs experience a sharp increase in activation overpotentials when CO is added to the anode stream. The CO overpotential increases more steeply at low current densities for the UMD MEA. However the overpotential also levels off much more sharply as CO oxidation begins to occur, so that the UMD MEA equals and then surpasses the BASF MEA in performance at 0.55 V at 25 ppm CO, down to 0.45 V at 500 ppm.

The performance of the BASF MEA is more consistent with the literature [6, 12], where PtRu *V*-*i* curves generally do not show a sudden shift in slope at the onset of CO oxidation, but continue to decline gradually. The shape of the UMD curves resembles those of MEAs with pure Pt as the anode electrocatalyst, which shows a similar increase in activity at CO oxidation potentials around 0.7–0.8 V

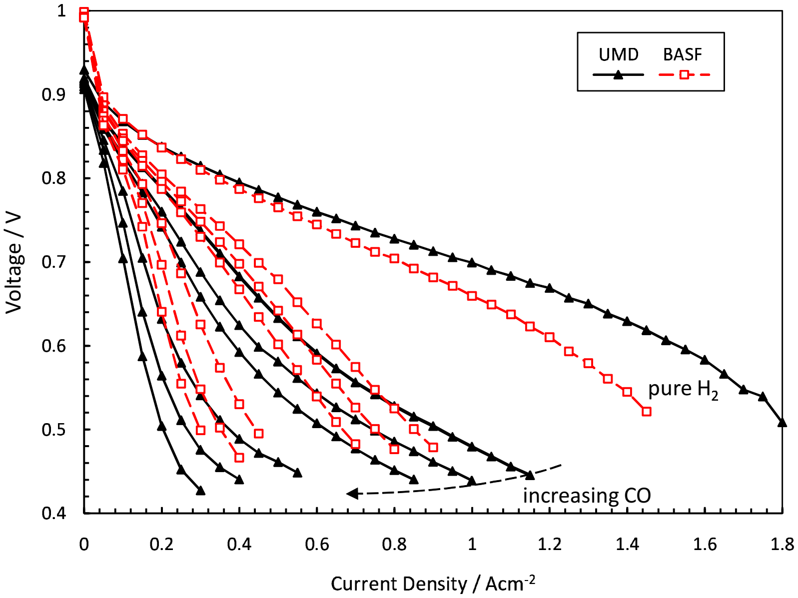

Figure 2.6: Polarization curves of a commercial BASF MEA compared to an in-house fabricated MEA using identical components (UMD). Both MEAs were tested with H_2 and 25, 50, 100, 250, 500, and 1000 ppm of CO on the anode, air on the cathode, at 70 °C, 2 bar gauge backpressure, and fixed stoichiometry of 2.2 on both sides.

overpotential. However, the performance of the UMD MEAs is far superior to that of MEAs with pure Pt anode electrocatalysts, and will be further discussed in the following chapter.

Sample galvanostatic impedance spectra measured from a UMD PtRu MEA during regular H_2/air testing are plotted in Figure 2.7. The steady-state current density was selected to lie in the linear region of the V-i curves as shown in Figure 2.6 and oscillations were 10% of the steady-state amplitude. Bulk resistance, measured between the y-axis and leftmost x-intercept, remains constant as CO is introduced to the anode and increased up to 250 ppm, consistent with current-interrupt resistance measurements.

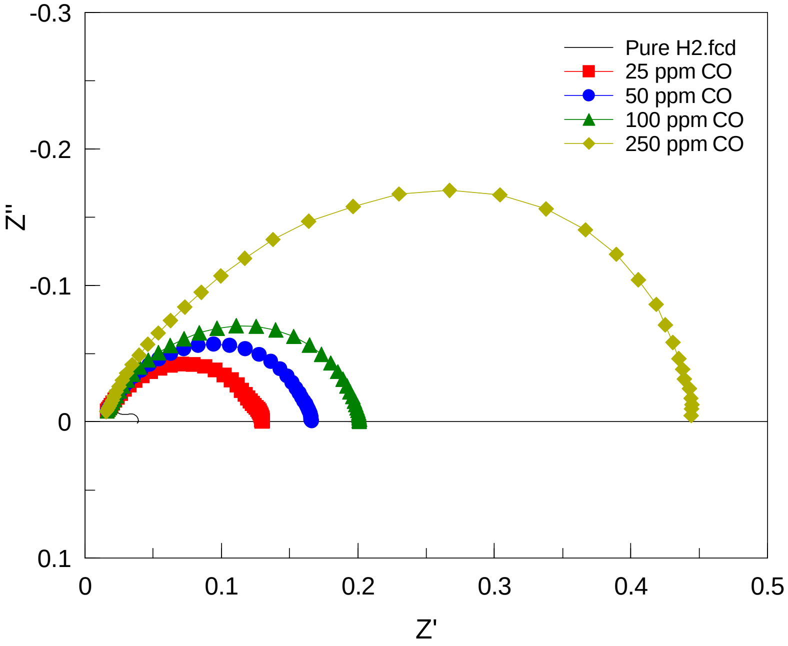

Figure 2.7: Galvanostatic EIS of a UMD PtRu MEA, with pure H_2 and CO concentrations up to 250 ppm on the anode and air on the cathode . Current densities were fixed in the ohmic region of the V-i curve at each CO concentration.

Figure 2.8 shows two cyclic voltammetry scans of a PtMo MEA. CV and CO stripping experiments were attempted on several different MEAs. Hydrogen desorption and adsorption regions are visible in this figure and CO stripping peaks were also observed. However peaks were not well defined and results were not reproducible. Difficulties were mostly likely related to H_2 crossover or residual H_2 remaining on the anode even after up to 2 hours of N_2 purging before scans. Thus, CV was not useful for calculating electrochemically active surface areas (ECSA) for the catalysts, which would have been useful in comparing the catalyst layers and normalizing the activities.

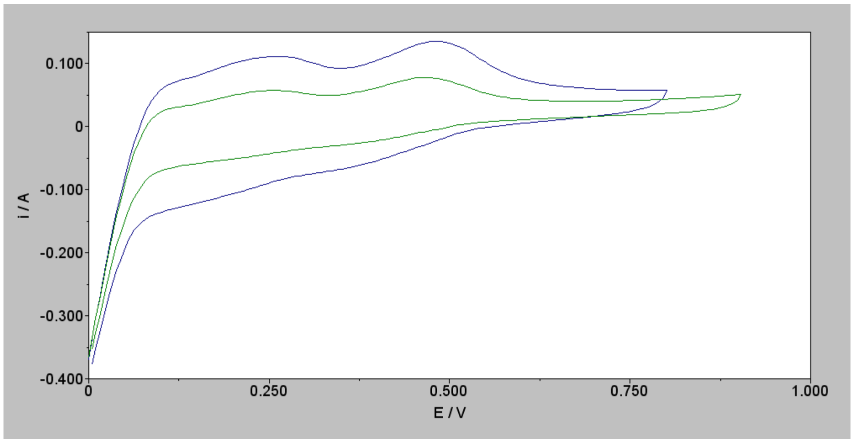

Figure 2.8: Cyclic voltammetry of a PtMo MEA operated with N_2 on the anode and H_2 on the cathode. Scans were conducted at room temperature at a scan rate of 20 mV/s.

Chapter 3

Comparison of PtMo and MoO_x@Pt MEA Performance

Previous RDE studies [25] suggest that in CO-laden acidic solutions MoO_x@Pt core-shell electrocatalysts have extremely low CO overpotentials due to the MoO_x core altering the Pt surface favorably for enhanced CO oxidation. While it is claimed that RDE experiments are adequate measures of electrocatalyst performance in full PEMFC MEAs for O_2 reduction on the cathode [50], it is not known whether that lower CO oxidation overpotentials in RDE experiments translate into better anode performance in MEAs. This motivated single-cell MEA testing of the promising MoO_x@Pt and PtMo electrocatalysts to corroborate the RDE results.

In addition to high HOR activity and CO tolerance, durability and cost are also critical factors that must be considered when developing catalysts for practical use. Material costs of the catalyst are currently a significant portion of the stack cost, so reductions in precious metal content and catalyst loading will be critical in lowering the price of PEM fuel cell systems [50]. Sintering and agglomeration of catalyst particles can reduce the electrochemically active surface area of the catalyst and decrease utilization over time [51], and the harsh operating environments in the cell can also lead to leaching or degradation of the catalyst structure, lowering activity.

This chapter presents results of MEA testing with PtMo alloy and MoO_x@Pt core-shell electrocatalysts fabricated at the University of Maryland. Polarization performance in pure H_2 and CO concentrations up to 1000 ppm is analyzed and compared to a baseline CO tolerance provided by MEAs fabricated using a commercial PtRu catalyst. Performance of the three catalysts is also assessed on a precious metal content basis. Finally, performance stability and durability of the catalysts are investigated over up to 9 days of continuous testing as well as post-testing examination by TEM and EDX.

3.1 MEA Performance

Unless otherwise specified, in this chapter "PtRu" refers to to the 1:1 alloy catalyst purchased from BASF, "PtMo" is the $Pt_{0.8}Mo_{0.2}$ alloy catalyst, and MoO_x@Pt is the core-shell catalyst. Both Mo-containing catalysts were fabricated in-house. The complete MEAs with PtRu as the anode electrocatalyst that were purchased from BASF were used solely for the purpose of validating the MEA fabrication process as shown in Chapter 2 and will not be discussed further.

3.1.1 H_2 Polarization

The H_2 polarization curves for PtRu, PtMo, and MoO_x@Pt are plotted in Figure 3.1. Testing conditions are shown in Table 2.2 and were held constant between catalysts. While previous comparative studies have found little difference between the H_2 performance of PtRu anode electrocatalysts and co-deposited Pt/MoO_x [18] and $Pt_{0.5}Mo_{0.5}$ alloy [6] anode electrocatalysts, in this study the MEAs with PtRu anode catalysts consistently exhibit higher H_2 performance than the MEAs with the

PtMo alloy or core-shell anode electrocatalyst. Both Mo-containing MEAs display large activation overpotentials at current densities below 0.1 A·cm^2, compared to the PtRu MEA. Since the anode GDL, membrane, and cathode GDE are the same for all the MEAs, the differences likely originate from the performance of the anode catalyst layers. From Equation 1.7 it can readily be seen that higher η_{act} corresponds to a low exchange current density i^0. However both PtMo and MoO$_x$@Pt demonstrated extremely high activity in RDE studies, implying that the loss of activity in MEAs results from poor catalyst utilization.

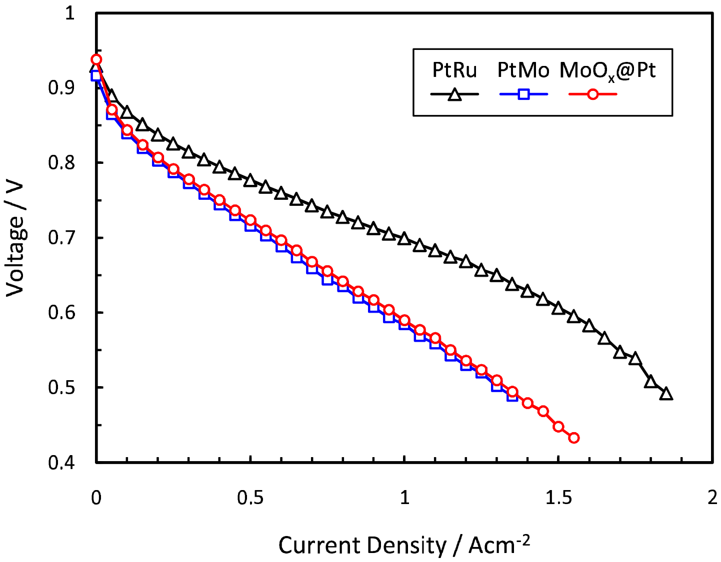

Figure 3.1: H$_2$ V-i curves for MEAs fabricated with PtRu, PtMo, and MoO$_x$@Pt.

All catalysts were 30 wt% metal supported on XC-72 porous carbon particles. However, it is unknown what treatments were applied to the commercial carbon support prior to deposition of the PtRu. Heat or chemical treatment of the carbon support can have a strong impact on catalyst distribution and active surface area [52, 53], so any treatment of the PtRu support, as opposed to the untreated XC-72 used for the two Mo-containing catalysts, could partially account for lower catalyst utilizations and H_2 performance.

Another variable possibly contributing to the large variation in the anode electrocatalyst H_2 performance in MEA testing involves catalyst preparation methods and the influence of residual stabilizers on the catalyst-ionomer interface. The PtMo alloy nanoparticles were heat-treated after synthesis to remove the oleic acid capping agent and leftover surface contaminants. On the other hand, heat treatment was not performed on the MoO_x@Pt to avoid damaging the core-shell structure, thus leaving substantial amounts of PVP stabilizer on the particle surface (TGA suggests that PVP adds 40% to the MoO_x@Pt weight; this is accounted for in the MEA catalyst loading as described in Chapter 2). It is not known what treatment the BASF catalyst may have undergone and if there are any residuals on the PtRu surface. While residuals did not appear to negatively impact earlier thin-film RDE experiments where the three catalysts demonstrated nearly identical H_2 activities [25], the capping agents may have a significant impact on the catalyst-ionomer interface, as seen in differing particle agglomeration effects in the catalyst inks and likely resulting in variations in the MEA catalyst layers.

3.1.2 Ohmic Polarization

Effects of variations in catalyst layer structure can be observed via the area specific resistances (cell resistance normalized by the area) of six MEAs, two containing each catalyst, plotted in Figure 3.2a versus current density. Bulk, or ohmic, resistance of the single cell is measured by the current-interrupt method during all tests, and includes resistances due to ionic conduction through the membrane and membrane-catalyst interfaces, as well as resistances of electronic conduction through the catalyst layer, GDLs, current collectors, and their interfaces. Of these components, only the anode catalyst layer is changed between MEAs, and so variations are primarily due to the structure of the catalyst layer and the quality of electrical conduction through carbon particles.

Two plots of current-interruption measurements are shown for each catalyst, from two MEAs that were fabricated at the same time and from the same batch of catalyst ink, demonstrating the reproducibility of the fabrication process. ASR varies by less than 4% within each pair. The figure shows that the PtRu catalyst layers have the lowest resistance, followed by the PtMo ink A, then the MoO_x@Pt core-shell. An additional curve for an MEA fabricated from a different, more dilute, batch of PtMo ink (ink B), illustrates that inks do impact catalyst layer performance: the ASR of an MEA fabricated from PtMo ink B is 10 $m\Omega\cdot cm^2$, or 15%, greater than that of a PtMo ink A MEA. However, these variations in resistance have little effect on overall MEA performance; at 1 $A\cdot cm^{-2}$ the ohmic overpotential for the PtMo B MEA is only 12 mV greater than that for the lower PtRu MEA. Figure 3.2b also demonstrates that there is negligible change in the bulk resistance when CO is introduced into the anode feed stream.

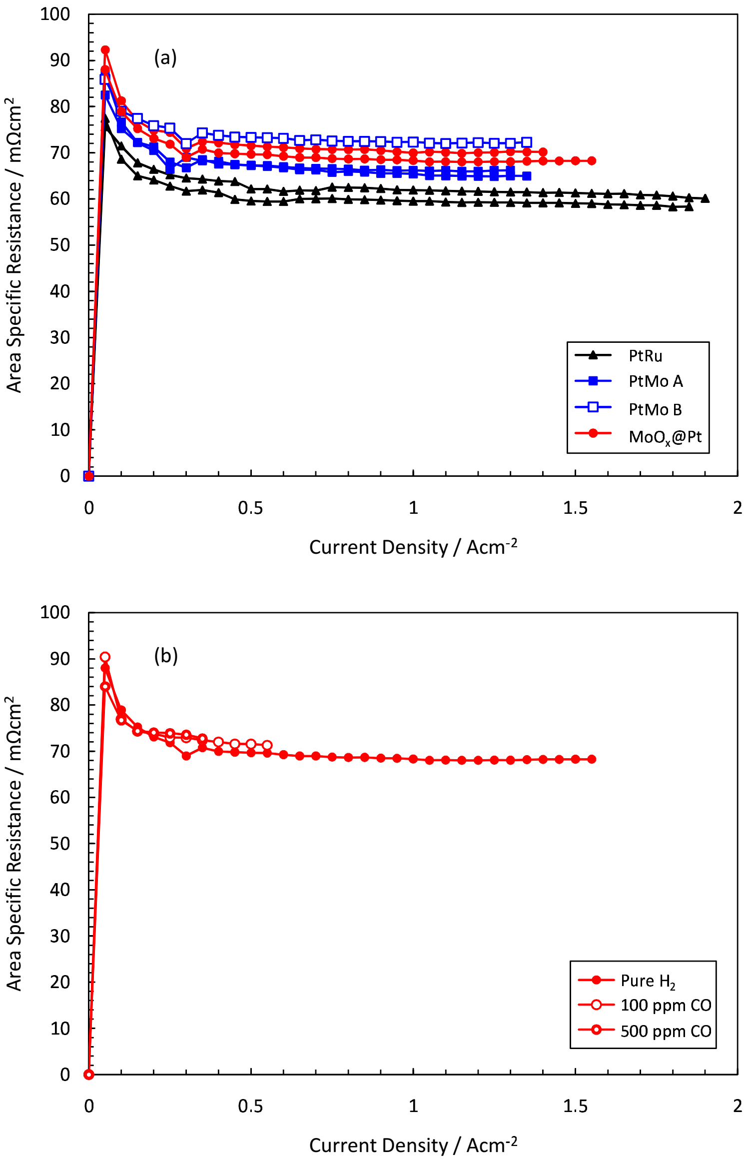

Figure 3.2: Area specific resistance (ASR) versus current density, (a) in pure H_2, for MEAs fabricated from each catalyst and from two different batches of PtMo ink, and (b) of a MoO_x@Pt MEA in pure H_2 and 100 ppm CO.

3.1.3 CO Polarization

Polarization curves for in-house fabricated MEAs with PtMo (left, (a) and (b)) and MoO_x@Pt (right, (c) and (d)) anode electrocatalysts are shown in Figure 3.3 for various concentrations of CO in H_2 in the anode feeds. The performance of both Mo-containing catalysts is compared to the commercial PtRu electrocatalyst. As indicated in Figure 3.3, while the BASF PtRu catalyst has the best pure H_2

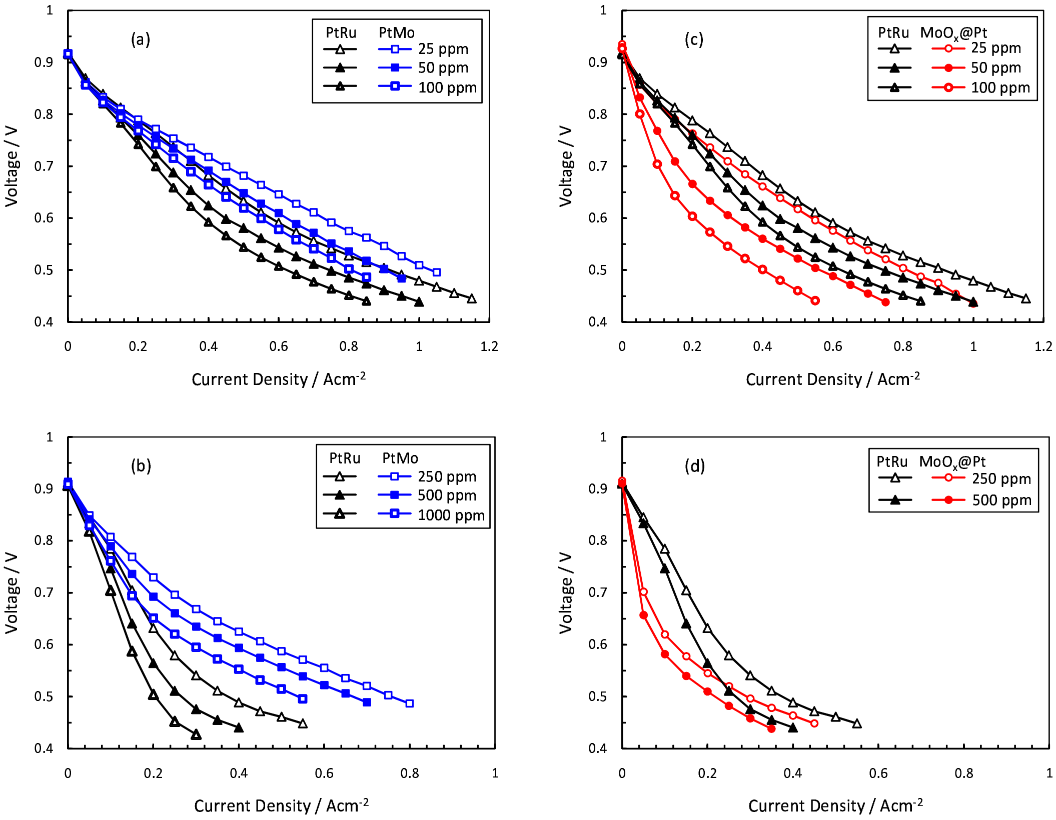

Figure 3.3: *V*-*i* curves of comparable MEAs at 70 °C with different anode electrocatalysts for a range of CO concentrations in H_2 anode feeds: a) and b) PtRu and PtMo anode electrocatalysts in 25, 50, 100, and 250, 500, and 1000 ppm CO in H_2, and c) and d) PtRu and MoO_x@Pt in 25, 50, 100, and 250 and 500 ppm CO in H_2.

performance (seen in Figure 3.1), the PtMo alloy exhibits significantly higher CO tolerance for all CO concentrations tested up to 1000 ppm. This enhanced performance over PtRu is consistent with earlier studies by others where the catalysts were prepared by different methods [6, 18]. Additionally, the PtMo catalyst avoids the steep activation overpotential at low current densities preceding the onset of CO oxidation that is evident in the PtRu curves, as signaled by a drop in the slope of the V-i curve. This rather gradual activation for CO oxidation was also observed for the PtMo electrocatalysts in the RDE experiments.

On the other hand, the MoO_x@Pt exhibits large activation overpotentials for anode CO concentrations above 25 ppm as shown in Figures 3.3c and 3.3d. For the higher CO concentrations, performance drops so sharply that testing was terminated at 500 ppm CO rather than 1000 ppm. MoO_x@Pt does show a dramatic drop in polarization resistance when the cell voltage drops below 0.6 V. However, the MEAs with the MoO_x@Pt anode catalyst do not perform as well as either the PtRu or the PtMo alloy electrocatalysts except at extremely high current densities where the cell voltage is less than 0.5 V.

The poor performance of MoO_x@Pt electrocatalyst stands in contrast to the prior RDE results, which showed superior H_2 in the presence of CO for the core-shell versus the two alloys. However, the initial large activation overpotentials as well as the reduced H_2 performance give a strong indication that the MoO_x@Pt electrocatalyst surface is not being fully utilized. This poor surface utilization suggests an impact of the stabilizing surfactant on the catalyst activity, either due to site blocking or disruption of the catalyst-ionomer interface for effective charge transfer. This suggests the need for further research on strategies for removing particle stabilizers after synthesis which has been identified as a significant challenge for nano-architectured catalyst development [54].

Discrepancies between RDE and MEA performance can be attributed mainly to mitigating effects of the liquid electrolyte on PVP-caused disruptions to the catalyst-ionomer interface in RDE experiments. However, the lack of liquid electrolyte in the MEA environment could allow more unfavorable interactions between the PVP and ionomer. Additionally, an approximately 6-fold increase in Nafion loading between the thin-film RDE and MEA electrodes could exacerbate problems with the Nafion/carbon-supported catalyst interface, amplifying differences that were not observed in thin-film catalyst layers.

Figure 3.4 provides an alternative summary of the performance of the three catalysts at typical fuel cell operating conditions 0.6 and 0.7 V. As indicated in the plots, the PtMo alloy clearly shows superior performance with power densities as high as 0.25 $\mathrm{W{\cdot}cm^{-2}}$ in 500 ppm CO at 0.6 V. This high CO tolerance for the PtMo alloy anode catalyst indicates the potential for system integration of a PEM fuel cell with a hydrocarbon reformer with only minimal CO clean-up if the anode performance with this electrocatalyst can be demonstrated to have adequate long-term durability.

Figure 3.5 replots some of the V-i curves in Figure 3.3 in terms of an effective CO overpotential, η_{CO}, the voltage drop caused by the presence of CO in the anode feed. η_{CO} is calculated for each CO concentration by subtracting the CO

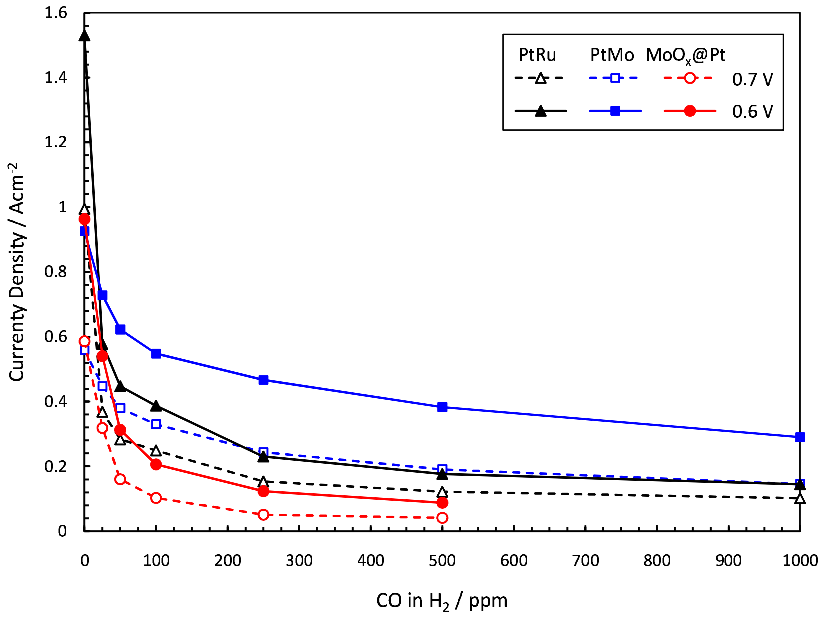

Figure 3.4: Current densities at 0.6 and 0.7 V in pure H_2 and CO concentrations up to 1000 ppm.

contaminated *V*-*i* curve from the pure H_2 curve as seen in Equation 3.1.

$$\eta_{CO} = V_{cell,H_2} - V_{cell,CO} \tag{3.1}$$

The CO overpotential is largely a measure of the increased activation overpotential for H_2 oxidation on the anode, caused by CO competing with H_2 for active sites on the catalyst. Concentration overpotentials should be unchanged due to the small mole fractions of CO, and Figure 3.2 shows that ohmic resistances do not depend on CO concentration. Cathode overpotentials and losses due to the anode catalyst layer structure are also independent of CO, and are accounted for by using the pure H_2 curve as a baseline.

Figure 3.5 clearly shows the transitions from a steep activation region at lower current densities to the rapid drop in polarization resistance with the onset of CO

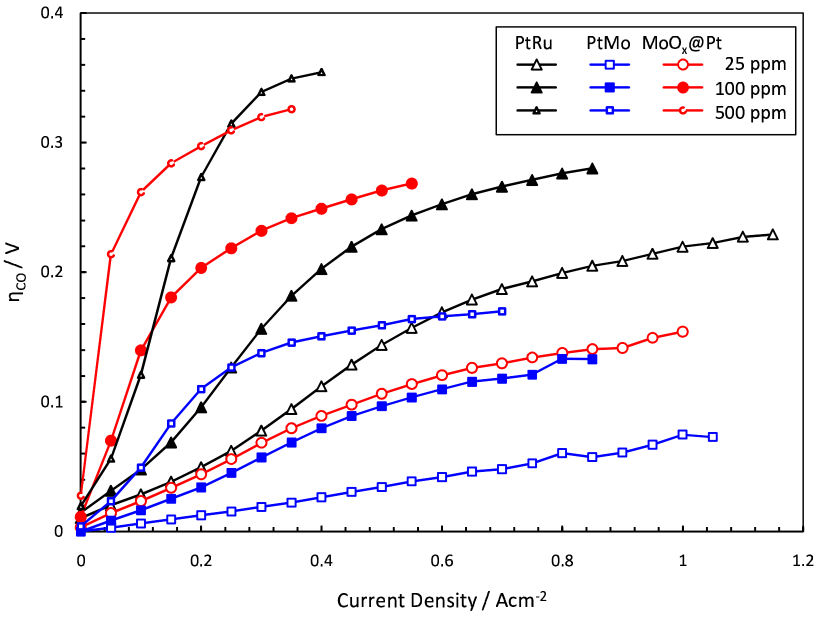

Figure 3.5: η_{CO} for the three catalysts in 25, 100, and 500 ppm of CO.

oxidation particularly for the core-shell and PtRu electrocatalysts. At the highest CO concentrations shown in Figure 3.5 (500 ppm), the apparent onset of rapid CO oxidation begins at η_{CO} around 0.12 V for the PtMo, 0.28 V for MoO$_x$@Pt, and 0.34 V for PtRu. These results indicate the effectiveness of Mo-containing electrocatalysts for tolerating high levels of CO in the anode stream, relative to commonly used PtRu catalysts, for low-temperature PEMFC applications.

3.1.4 Precious Metal Loading

On a per membrane area or total catalyst loading basis, the order of performance for CO tolerance of three anode electrocatalysts CO can be generally stated as PtMo alloy, PtRu alloy, and MoO$_x$@Pt core-shell. However, the MoO$_x$@Pt catalyst uses less precious metal (PM) than the PtMo alloy catalyst, and both Mo-containing catalysts have reduced PM content compared to the PtRu alloy. Since it is desirable to reduce PM loadings in PEM fuel cells in order to lower material costs, Mo has the potential to be a more cost-effective choice for combining with Pt than Ru if the Mo-containing catalysts can be shown to maintain stable operation.

To assess instead performance on a per gram of anode PM basis, the catalysts used in this study were carefully characterized by a variety of methods, so that their structure and composition are well-known as discussed in the previous reference [25]. The characterization indicated that the PtMo alloy contains 80% Pt and 20% Mo on a molar basis while the MoO$_x$@Pt core-shell consists of 40% Pt and 60% MoO$_x$ on a molar basis. Weight percentages are shown in Table 3.1.

Table 3.1: Elemental composition of the PtRu, PtMo, and MoO$_x$@Pt nanoparticles, showing atomic ratios and weight percents. Precious metals are in bold.

	Catalyst:	PtRu	PtMo	MoO$_x$@Pt
	Pt:X atomic ratio:	1:1	4:1	2:3
wt %	**Pt**	**66**	**89**	**73**
	Ru	**34**		
	Mo		11	22
	O$_x$			5

From these measurements effective PM loadings for each catalyst were estimated, and the *V*-*i* curves were replotted on an A·(mg PM)$^{-1}$ basis. Figure 3.6 shows the resulting *V*-i' curves at 0, 100, and 500 ppm of CO in H$_2$, where i' is the specific current or PM mass activity. As before, the PtMo alloy has superior CO performance at all concentrations of CO. However, due to its reduced PM content, the MoO$_x$@Pt electrocatalyst is has only slightly lower pure H$_2$ performance than the PtRu on a PM loading basis, and is more effective than PtRu in 25 ppm CO. At higher concentrations the steep activation overpotentials of the MoO$_x$@Pt catalyst cause its performance to fall below that of PtRu, but overall the CO tolerance of the MoO$_x$@Pt electrocatalyst is much more comparable on a PM loading basis. This suggests that if the currently observed impacts of residual surfactant from the core-shell synthesis can be reduced by more effective cleaning strategies, it is likely that the MoO$_x$@Pt electrocatalysts will show superior mass activity for all CO concentrations even if not on a total catalyst loading basis.

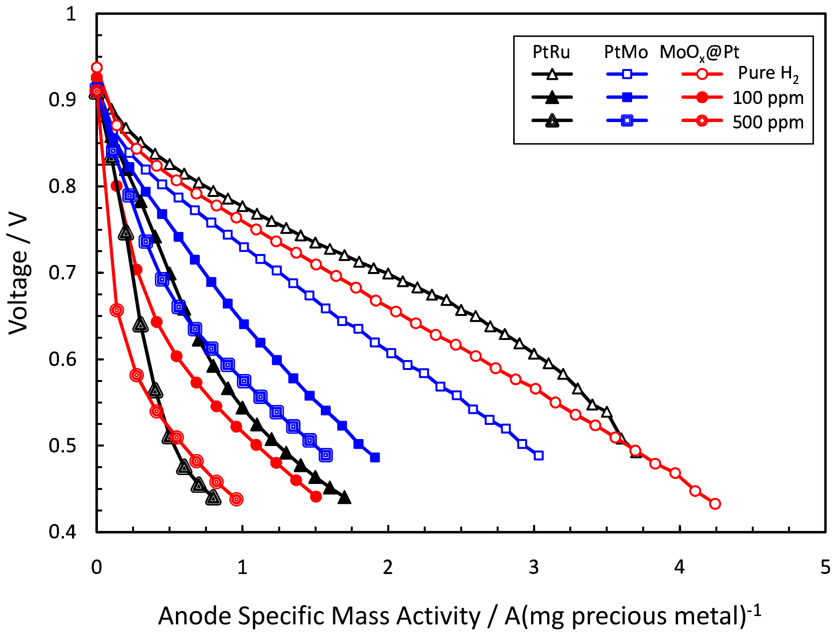

Figure 3.6: V-i' for PtRu, PtMo, and MoO$_x$@Pt at 0, 100, and 500 ppm CO in H$_2$. i' is the anode mass specific mass activity – current per mg of precious metal in the anode catalyst layer.

3.2 Catalyst Durability

A particular concern with Pt-Mo nanoparticle electrocatalysts is their long-term durability due to leaching and loss of the Mo in the acidic PEMFC environment as described in Chapter 1.2.2. Leaching from the anode catalyst can not only decrease catalyst activity and CO tolerance but also result in reduced electrolyte and cathode performance due to Mo contamination. Although there is a well-documented decrease in PtMo thin-film electrode and MEA performance as voltage is cycled [20, 21] as well as dissolution of the Mo from the anode into the electrolyte and migration to the cathode [19], it has also been noted that more homogeneous and crystalline PtMo alloys have less significant performance losses compared to amorphous mixtures [19, 23]. Additionally, less leaching was observed from catalyst incorporated into MEAs relative to thin-film electrodes in liquid electrolytes. These two effects support the stable performance of a PtMo over 2000 hours of operation observed by Mukerjee et al [6], and suggest that leaching may be mitigated by well-ordered alloys or core-shell catalyst architectures with a seemingly pure Pt surface.

3.2.1 MEA Performance Stability Testing

To assess this possibility for both the PtMo alloy and MoO_x@Pt core-shell anode catalysts, performance stability was investigated by holding the cell at 0.6 V in pure H_2 and 100 ppm CO for up to 5 days after initial testing, with V-i curves recorded periodically. Figure 3.7 shows the current densities of PtMo and MoO_x@Pt

MEAs over 72 and 60 hours of stability testing, respectively, as well as η_{CO} and ASR as a function of i at various points during the testing. In Figure 3.7, the Test 1 and 2 curves are from the first two days of testing, when polarization was measured in CO concentrations from 0 to 1000 ppm; the other curves are indicated by the amount of time after the start of stability testing. The Test 2 H_2 baseline was used to calculate all subsequent CO overpotentials. Stability testing was started immediately following a series of CO curves at 0–1000 ppm, and so initially the current density increased as the cell recovered from the higher concentration of CO to 100 ppm. The gaps in data and voltage spikes occur when polarization curves are measured. Smaller dips and spikes occur when water momentarily blocks the serpentine channels in the flow fields.

Performance at 0.6 V as shown in Figure 3.7 is quite stable for the PtMo alloy, but the CO overpotential curves show that the activity does change slightly over time with a general trend toward increasing activation overpotential for CO oxidation but a slight drop in polarization resistance at the high current densities. Current densities obtained with the MoO_x@Pt catalyst were lower than for the alloy, and the constant 0.6 V was interrupted every 4 hours for a polarization curve rather than every 2 hours. Fewer small current spikes from the MoO_x@Pt can be related to less water production at the reduced current density, but overall the MoO_x@Pt also exhibits a slow increase in activation overpotential over the 72 hours of stability testing. Interestingly, the core-shell exhibits an initial decrease in CO overpotential over the first three days of testing, unlike the alloy. After the first two days the MoO_x@Pt CO overpotential curves undergo a shift in slope and become flat at a

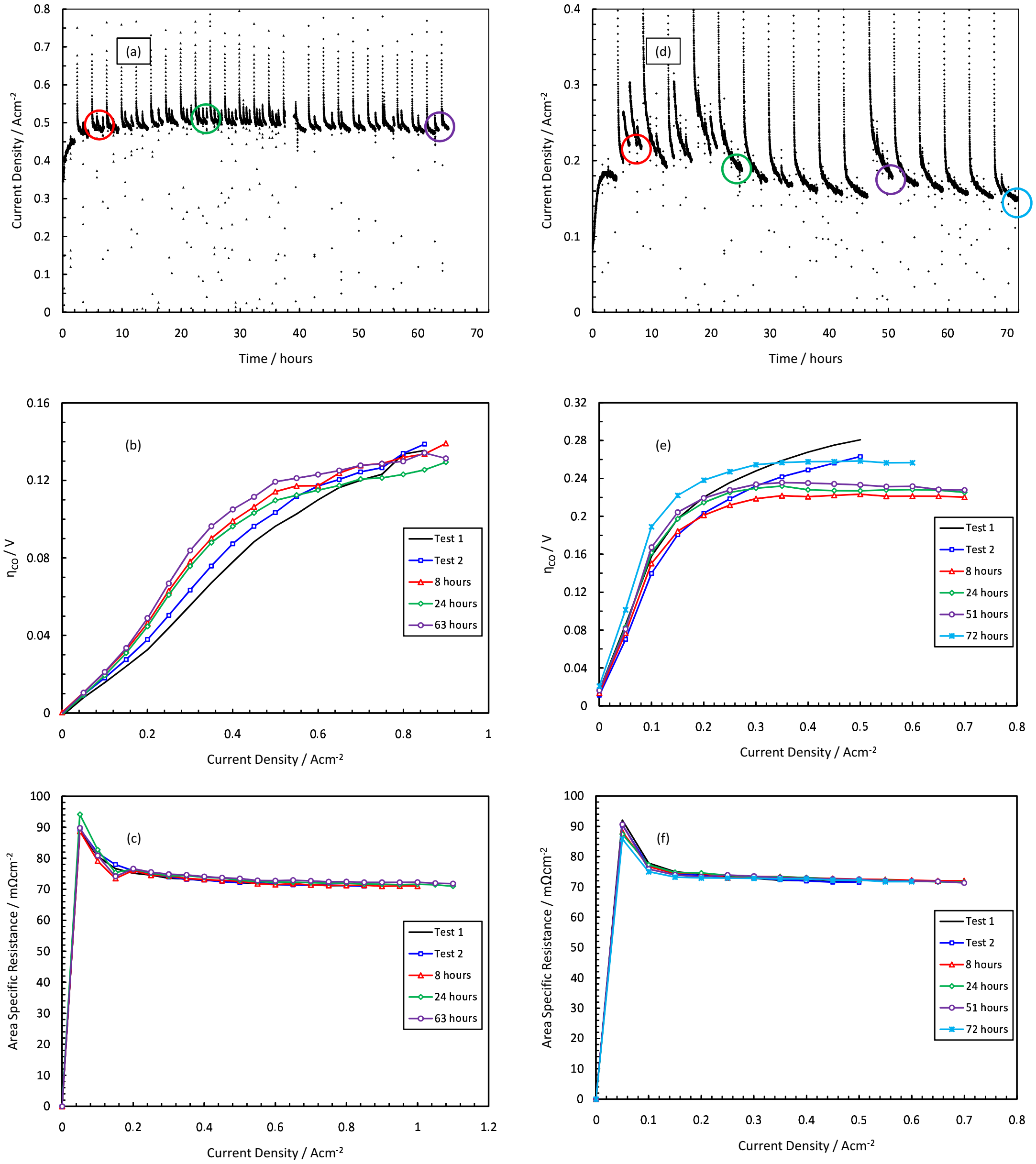

Figure 3.7: MEA stability testing at 70 °C cell operation. a) and d) Current density versus time while holding the cell at 0.6 V in 100 ppm CO for PtMo (left) and MoO_x@Pt (right). b) and e) CO overpotentials at various points during testing. c) and f) ASR at various points during testing. Test 1 curves are from the first day of testing in 25–1000 ppm CO, test 2 from the second day, hour 0 of stability testing begins after the 1000 ppm test on the second day.

cell potential of ~0.6 V. For both catalysts the ASR, shown in Figures 3.7c and 3.7f remains constant throughout the stability testing, indicating that 1) the η_{CO}s plotted in Figures 3.7b and 3.7e are representative of increased activation overpotentials due to CO, and 2) if any Mo leaching is occurring, it does not affect membrane hydration and thus conductivity as would be expected from [19]. The evolution of activation overpotentials over time could be due to changes in the oxidation state of the Mo; this could be verified through XPS.

3.2.2 Catalyst Stability Characterization

Both catalysts and MEAs were characterized by SEM, TEM, and EDX analysis. Figure 3.8 shows TEM images of carbon-supported catalyst removed from the anode after MEA testing was completed. TEM and EDX analysis show there is no significant change of particle size and composition after the fuel cell testing. The average composition after testing of the PtMo alloy catalysts remains at 80% by mole Pt and for the MoO_x@Pt core-shell catalyst the Pt to Mo ratio does not change significantly from its original pre-testing 40:60 ratio as shown in Figure 3.8. In addition, no serious particle aggregation or sintering was observed for the catalysts by SEM or TEM after testing, probabaly due to the strong particle-support interactions. However, these methods do not confirm if the architecture of the nanocatalysts remains intact.

While the post-TEM images do not reveal any evidence of anode electrocatalyst degradation, they do not fully address the issue of Mo leaching from the catalyst

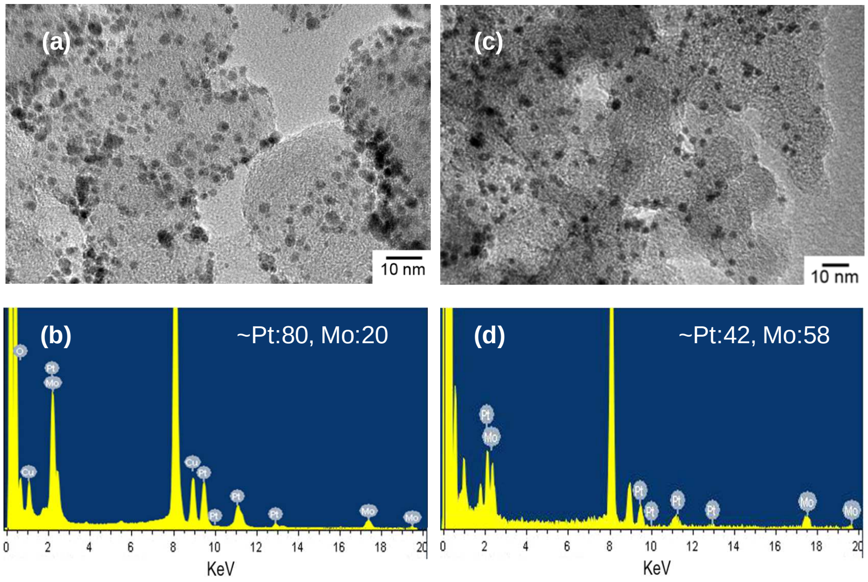

Figure 3.8: TEM images and EDX analysis of (a and b) PtMo alloy after 9 days of testing in H_2 + CO anode feeds, and (c and d) MoO_x@Pt after 7 days of testing in H_2 + CO anode feeds.

layer into the electrolyte. To explore this issue, SEM-EDX line scans of untested (dashed) and post-testing (solid) PtMo MEA cross sections are shown in Figure 3.9. SEM-EDX results are not fully quantitative in that only relative signal strengths are obtained for each element present in a sample. The two MEAs were fabricated together and analyzed after one had undergone 9 days of testing; the other was not tested. Length scales were normalized to the Nafion membrane thickness (the membrane of the tested MEA was slightly thicker, possibly due to swelling in the humidified test conditions), and signal strength was scaled by setting each cathode platinum peak to 100. While the data in Figure 3.9 are only semi-quantitative, there is evidence of leaching of Mo into the Nafion and across to the cathode during fuel cell operation. This is indicated by the slight increase in Mo signal strength in the membrane and cathode regions relative to the untested MEA. The non-zero Mo baseline visible in the untested sample is likely due to a peak overlap with sulfur [55].

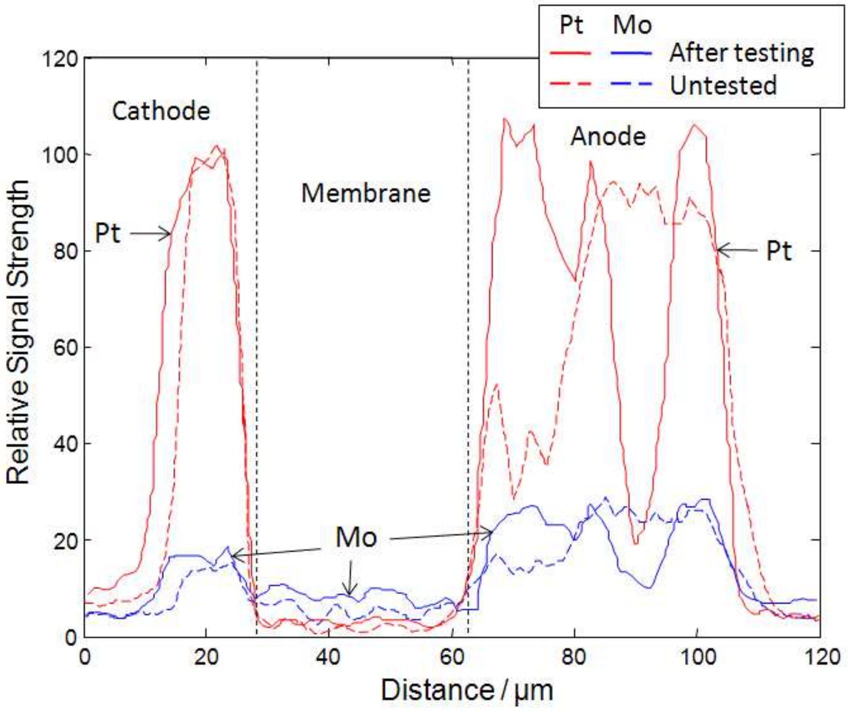

Figure 3.9: SEM EDX line scans of untested (dashed) and post-testing (solid) PtMo MEA cross sections, showing Pt and Mo content distribution in the membrane and electrodes.

Figure 3.10 compares the same post-testing PtMo MEA to a MoO_x@Pt MEA that was tested for 7 days. These results are also not fully quantitative, since no untested core-shell MEA was available for comparison. Nonetheless, the line scans indicate that Mo signal strengths in the membrane and cathode are slightly lower in the core-shell MEA than in the alloy MEA, with the electrolyte having near ground level signals using the GDLs as a baseline. This supports expectations that the core-shell will reduce leaching due to the protective Pt layer and the oxidized nature of the Mo. Further long-term testing and more quantitative analysis must be pursued to ensure the durability of these electrocatalysts before they can be implemented into expensive PEMFC stack development efforts.

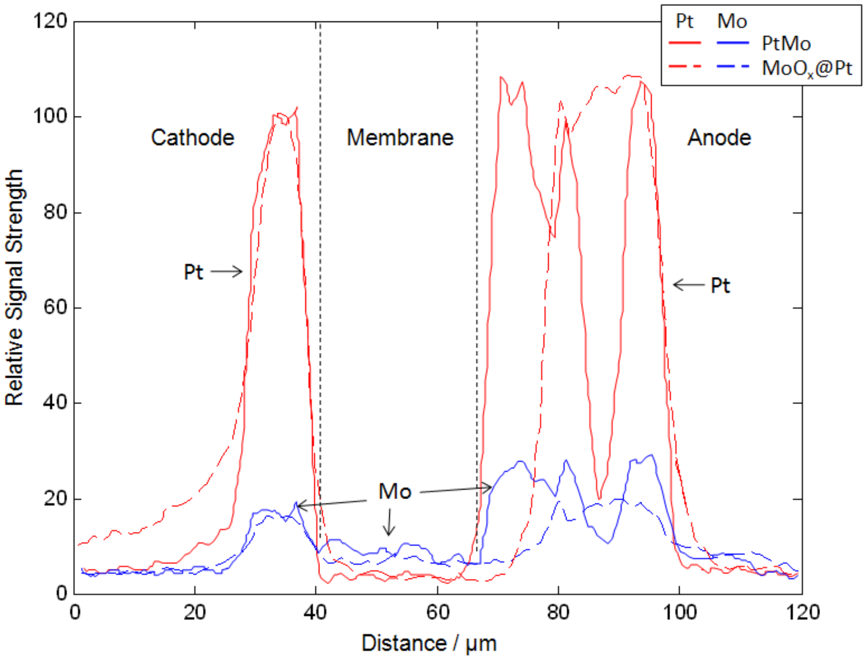

Figure 3.10: SEM EDX line scans of PtMo (solid) and MoO_x@Pt (dashed) MEA cross sections, showing Pt and Mo content distribution in the membrane and electrodes.

Chapter 4

Modeling Impacts of CO Tolerance on PEMFC System Performance

The CO tolerant electrocatalyst development efforts described in previous chapters are motivated by the desire to expand the market for PEM fuel cell systems, specifically liquid hydrocarbon-fueled gensets for portable/mobile applications. Such systems are attractive in terms of compatibility with current fuel infrastructure as well as offering quiet and low-emissions operation, and the potential for significantly higher efficiencies compared to current diesel technology. However, the size, complexity, and especially the cost of fuel cell systems must be further reduced in order to be commercially viable outside of niche markets. This chapter explores the impact of current-day and potential advances in CO tolerance on the system performance of a low-temperature PEM fuel cell system operating in conjunction with a hydrocarbon autothermal reformer and a preferential CO oxidation reactor for CO cleanup.

A system-level model for a liquid-fueled PEM fuel cell system with a 5 kW maximum power output is used to study how CO tolerance affects tradeoffs between the fuel cell, fuel processor, and balance of plant components. Empirical CO tolerant stack models are based on the performance of the PtMo alloy electrocatalyst presented in Chapter 3. As CO tolerance is increased over this current state-of-the-art Pt alloy catalysts, system efficiencies improve due primarily to higher fuel cell voltages and to a lesser extent to reductions in parasitic loads. Furthermore, increasing the CO tolerance of anode electrocatalysts allows for the potential for reduced system cost and complexity with minimal efficiency penalty by reducing PROx CO selectivity and conversion requirements.

4.1 System Model Description

The system flow diagram and component integration for a hydrocarbon-fueled PEM fuel cell generator is illustrated in the schematic of Figure 4.1. This study focuses on this particular configuration, which integrates a PEM fuel cell stack with a liquid-fueled autothermal reformer (ATR) with a water-gas-shift (WGS) reactor and a subsequent PROx reactor with proper thermal management for H_2 cleanup. Additional balance-of-plant components which draw parasitic loads are also illustrated in Figure 4.1 with the dominant parasitic loads coming from the air compressors for the ATR, fuel cell cathode, and the PROxreactor, and from the radiator fan. Electric motors and inverters for power conversion are not shown in Figure 4.1, and are modeled with constant efficiencies of 90 and 93% respectively.

Components for the cathode-side air supply, fuel reforming, exhaust and cooling are identical to those presented in an earlier study by Pearlman et al with a similar modeling approach [37]. The key difference is the replacement of the Pd membrane purifier in that previous study with a PROx reactor and associated air compressor and heat exchanger to cool the PROx effluent before it enters the fuel cell. Also, the Pd membrane purification implementation was previously integrated

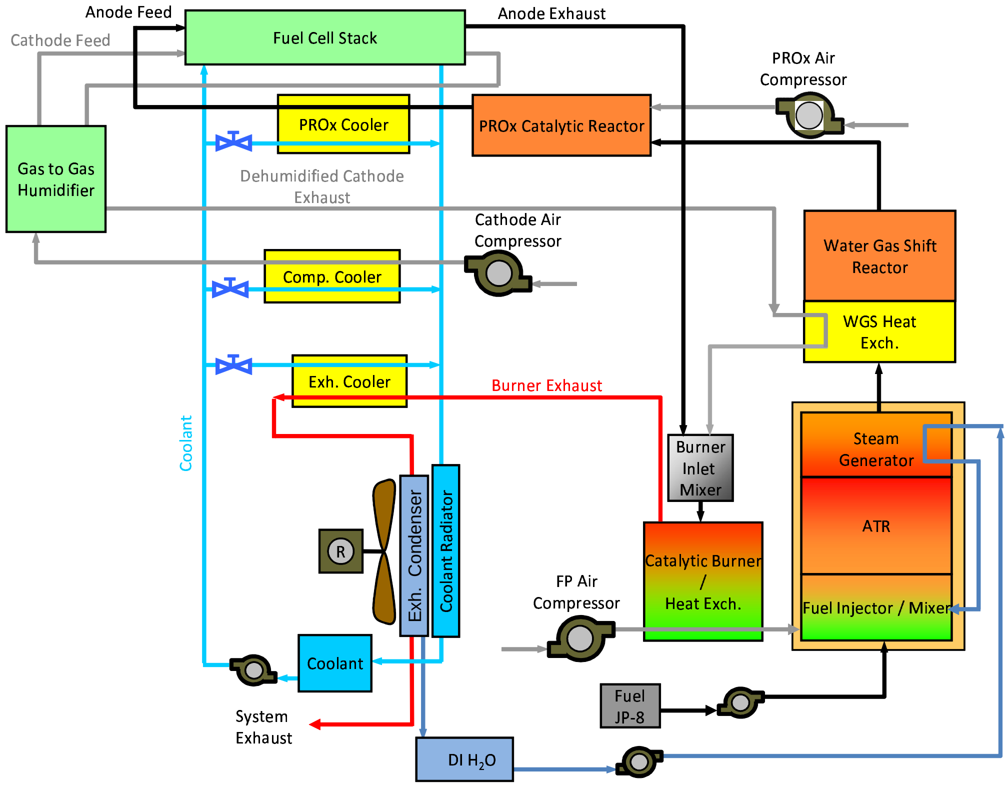

Figure 4.1: Flow diagram showing schematic of the hydrocarbon-fueled PEM fuel cell system modeled in this study with fuel processor, PROx reactor, catalytic exhaust burner, liquid-cooled fuel cell stack, and exhaust condenser for water recovery.

into the water-gas-shift reactor, while now the WGS reactor is just the reactor at the end of the fuel processor as shown in Figure 4.1.

4.1.1 Fuel Processor and CO Clean-up

The fuel processor is an autothermal fuel reformer (ATR) operating on a model kerosene (or JP-8), represented as $C_{12}H_{23}$ [37]. The ATR is maintained at constant steam-to-carbon ($S/C = 1.6$) and oxygen-to-carbon ($O/C = 0.8$) ratios in this study. This condition is mildly exothermic and has been shown to have adequate oxygen atoms to avoid significant carbon deposition in the reformer [56]. One key benefit in utilizing PROx for the CO cleanup is the relatively low operating pressure for the ATR and thus the reduced parasitic load associated with compressing the air for the reformer. In the current study, the ATR model assumes outlet flows based on full fuel conversion and equilibration of the WGS reaction at the high outlet temperature. The outlet temperature and equilibrium H_2, CO, CO_2, and H_2O mole fractions are found through an iterative solution of the coupled energy and species balances in the reactor. With complete fuel conversion, all carbon in the reformate stream is assumed to exit as either CO or CO_2. The small percentage of CH_4 and other hydrocarbons (<1.0% total on a wet basis [1]) observed in ATR exhaust is not considered here. After the ATR effluent is cooled by an intermediate steam generator (for the reformer itself), the reformate passes through a 4-stage WGS reactor, which is assumed to be sufficiently large to achieve equilibrium down to 300 °C. Intermediate cooling between the ATR and WGS reactor is critical to attaining lower exhaust temperature from the WGS and thus reduced CO concentrations. The WGS effluent is cooled through mixing with air from the PROx compressor before entering the PROx reactor at temperatures favorable for CO conversion. The PROx reactor is modeled by assuming a fixed CO conversion and selectivity. For the current study, CO selectivity is generally held at a baseline value of 85% based on advanced PROx reactors presented in the literature [57]. PROx CO conversion is generally fixed at a baseline of 99% although increased anode tolerance of CO encouraged studies looking at the effects of reduced CO conversion (90%) on system performance.

4.1.2 Fuel Cell Stack

For the fuel cell stack, the model follows the earlier study where an empirical polarization curve is adapted from a study of a Ballard Power Systems fuel cell stack [58]. The open circuit voltage is shifted up or down based on changes in the Nernst potential with changes in reactant partial pressures and temperatures. In this study, the pure H_2 voltage versus current density (V-i) curve is modified based upon the amount of CO in the anode feed. To this end, V-i curves for MEAs with relatively CO tolerant PtMo alloy electrocatalysts are derived from experimental results with simulated reformate streams. Curves are obtained at 25, 50, 100, 250, 500, and 1000 ppm CO in H_2, at intervals of 50 $\mathrm{mA \cdot cm^{-2}}$. These results (presented in Figure 3.3) are used to model the CO overpotentials as a percent drop from the reference hydrogen curve as a function of i. Linear interpolation is used between points and extrapolation beyond 1000 ppm. A CO-adjusted voltage V_{cell} is calculated for each desired current density and anode CO concentration from the PROx reactor. To further investigate the effects of CO tolerance, a CO tolerance factor, ξ_{CO}, is introduced, which reduces the CO penalty to that of a lower CO ppm value equal to the original CO ppm divided by the tolerance factor. For example, a CO tolerance factor of 10 indicates that the polarization curve data obtained at 25 ppm is assumed to be effective at 250 ppm. As such, this provides a convenient means for investigating the system-level benefits of future advances in CO-tolerant anode electrocatalysts for the low-temperature PEM-fuel cell systems relying on liquid-fuel reforming and PROx reactor CO-cleanup.

4.1.3 Balance of Plant

For the remainder of the balance of plant (BOP) components, the heat exchanger, compressor, and pump models approximate actual performance of components used in assembly of a working prototype of a liquid-fueled PEM fuel cell generator a tthe University of Maryland, and largely follow the earlier study. The reader is referred to that study for further details on heat transfer correlations for the heat exchanges and isentropic efficiency models for the compressors [37]. In the current study, more detail is given to modeling the coolant loop and the high-flow rate pump, and radiator fan power is taken from an experimental air flow rate versus power curve, to ensure that both the coolant pump and radiator fan parasitic loads are captured well in the model. In the PROx, cathode compressor, and exhaust heat exchangers as well as the fuel cell stack, the model calculates the heat transfer required to bring the gas streams to a set target temperature, then solves for the coolant flow rate needed to provide the desired cooling. More detailed heat loss models are also implemented in the current study in order to better examine temperature and thermal integration effects. Heat losses are modeled in the WGS reactor, PROx reactor, and radiator as a combination of natural convection and radiation heat transfer based on the average temperature of the component and T_{amb}. Heat loss calculations assume a constant overall heat transfer coefficient (U) value for convective losses and a constant emissivity for radiative losses. The losses were determined by fitting calculations to empirical heat loss estimates made during experimental testing of system components.

4.1.4 Implementation

As in the previous study, the model data is imported into MS Excel with a Visual Basic program running as a macro that determines steady-state operating conditions and system performance through a nested iterative sequence. The recycling of mass and heat flows, along with the feedback between system operating conditions and parasitic loads, requires such an iterative solution technique. The iterative loop is based upon stepping through each component and solving the nonlinear energy balance and species balance equations. The overall system power demand is then used to recalculate fuel, air, and coolant flows, and associated parasitic loads for system operation. Fuel flow rate to the system is determined iteratively through a species balance between available H_2 exiting the PROx reactor and the demanded anode feed at the desired H_2 stoichiometry (1.3 for all cases here). The new flow rates thus are used to update the parasitic loads, and gross power demand for the fuel cell stack is calculated from the sum of net (i.e., usable) power demand and the parasitic loads.

4.2 Model Results and Discussion

The current study does not explore the full system design space for a liquid hydrocarbon-fueled PEM fuel cell system, but rather focuses on the specific system illustrated in 4.1 operating at a baseline condition and variations from that baseline, primarily related to PROx conditions and anode CO tolerance. The baseline conditions and their range of variation in this study are given in Table 4.1, and key system parameters are shown in Table 4.2).

Table 4.1: Baseline conditions and modeled variations.

Parameter	**Baseline Value**	**Range**
Net electrical power output, $\dot{W}_{net}$ / W	5000	1000–5000
Ambient temperature, T_{amb} / °C	30	10–50
Anode CO tolerance factor, ξ_{CO}	1	1–10
PROx CO selectivity	0.85	0.75–1.0
PROx CO conversion	99%	90%-99%

Temperatures listed in Table 4.2 simply indicate limits placed on system components such that unrealistic operating conditions will not be found which give false impressions regarding overall system performance. The system studied here is designed to operate at a maximum power of 5000 W net electric power out. As indicated in Table 4.2, the system includes a relatively large fuel cell stack with area A_{cell}=300 cm^2 per cell and number of cells n_{cells}=75. Such a large stack is necessary to avoid the large anode overpotentials associated with non-zero CO concentrations at higher current densities. This allows for adequate voltages (and thus power densities) to be achieved even for the baseline CO tolerance when anode inlet CO concentrations rise to 200 ppm.

4.2.1 Ambient Temperature

The model was first run for a range of ambient temperatures using the baseline PROx reactor CO selectivity of 0.85 and CO conversion of 0.99, with fuel cell performance based on the current-day CO tolerance (derived from the experimental PtMo curves in Figure 3.3. The results for overall system efficiency and water balance at full (5000 W) and half (2500 W) power are shown in Figure 4.2a, which is presented such that the results can be readily be compared with the earlier study on a similarly-sized system using a Pd-membrane purification. As expected, increased cooling and other BOP loads lead to slight decreases in system efficiency and more significant decreases in net water balance with increasing T_{amb}.

Unlike in the Pd-membrane system study, here the water balance (water recovered from the exhaust condenser and fuel cell knockout flows minus the water demanded by the fuel processor as steam) remains positive even up to 50 °C. This is because there is no need for sweep steam as required in the Pd-membrane system [37]. Cathode humidification is accomplished by gas-to-gas water and heat exchange

Table 4.2: Critical system performance parameters.

Parameter	**Value**
Ambient Conditions:	
Temperature, T_{amb} / °C	30
Relative humidity	50%
Fuell cell conditions and properties:	
Operating temperature, T_{cell} / °C	70
Operating pressure / bar	1.35
Pressure drop across stack at 1 A·cm^{-2}	0.25
Stoichiometric ratio of cathode air flow	1.8
Stoichiometric ratio of anode H_2 flow	1.3
Fraction of H_2O produced in FC to anode	0.15
Number of cells per stack	75
Stack membrane area per cell / cm^2	300
Fuel reformer conditions:	
Inlet oxygen to carbon (O/C) ratio	0.8
Inlet steam to carbon (S/C) ratio	1.6
Max. inlet temperature / °C	500
Min. pre-heater approach ΔT / °C	20
Steam temperature out of generator / °C	125
Water-gas-shift reactor conditions:	
Min. equilibrium temperature / °C	300
PROx reactor conditions:	
Min. inlet temperature / °C	165
Balance of plant conditions:	
Radiator outlet coolant temperature / °C	60
Min. exhaust condenser ΔT / °C	10
Electric inverter efficiency	93%
Electric motor efficiency	90%

between the cathode exhaust and inlet flows. In fact, all conditions in this study showed adequate water recovery even with approach temperature differences in the exhaust condenser as high as 10 °C. Positive water balance is critical in remote, unmanned operation, especially in regions and climates where water may be scarce.

A key measure of system performance is overall system efficiency, η_{th}, which is defined here by Equation 4.1:

$$\eta_{th} = \frac{\dot{W}_{net}}{\dot{m}_{HC,in} h_{HC,comb}} = \frac{n_{cells} A_{cell} i V_{cell} - \dot{W}_{lost}}{\dot{m}_{HC,in} h_{HC,comb}} \tag{4.1}$$

The numerator is the power produced by the PEM fuel cell stack, minus the work lost ($\dot{W}_{lost}$) due to parasitic loads and motor and inverter inefficiencies, and the denominator is the lower enthalpy of the fuel consumed by the system to produce the desired net power. Figure 4.2a shows that η_{th} drops slightly with increasing T_{amb}, but generally remains around 24% at full power and 29% at half power. These efficiency values compare favorably to current state-of-the art diesel generators in this size range, and the fuel cell system also offers additional advantages in terms of emissions and noise. Even higher efficiencies should be achievable with improved reformer operating conditions and system optimization.

Some of the key system states helpful in understanding the variations in η_{th} are shown in Table 4.3. The first two columns illustrate how two effects combine to lower η_{th} at full power conditions compared to half power: 1) higher stack current density at full power leads to higher anode CO overpotentials as shown in Figure 3.5, and 2) higher WGS reactor outlet temperatures at full power result in higher CO concentrations entering the PROx reactor and subsequently the anode, which

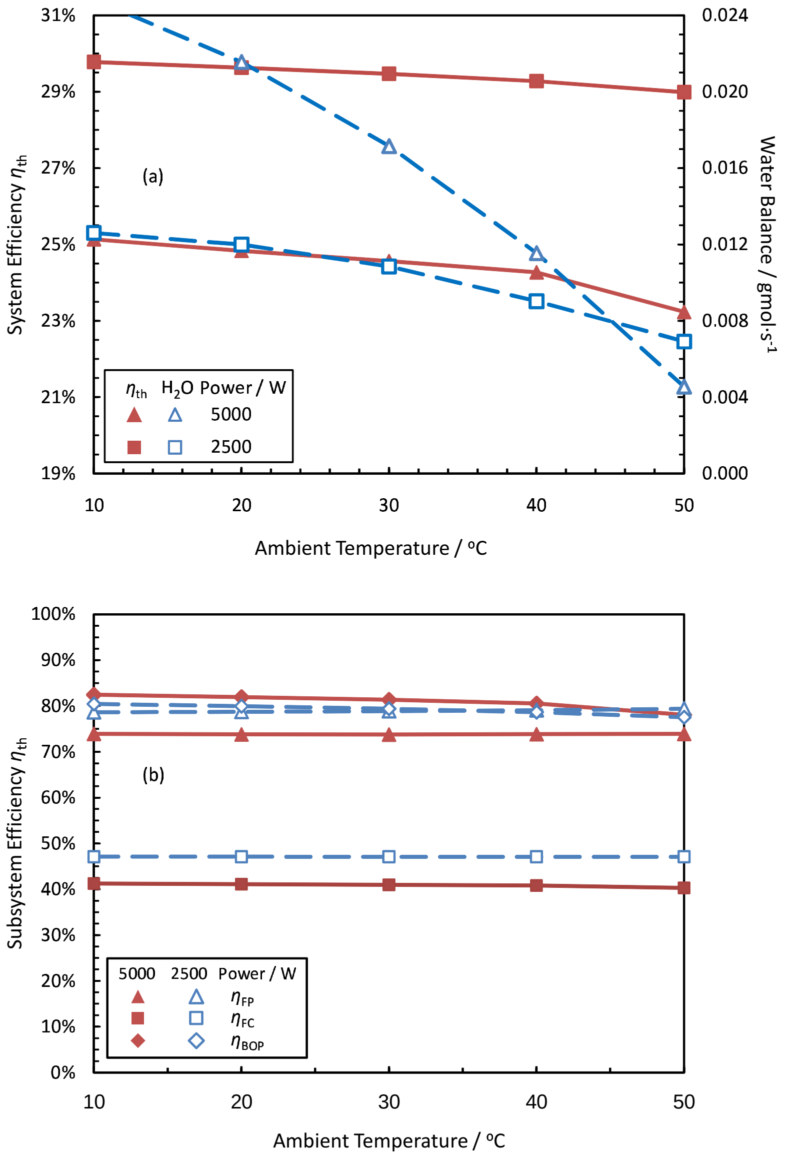

Figure 4.2: PEM fuel cell system performance versus T_{amb} at full and half power at baseline CO tolerance and PROx reactor conditions of 99% CO conversion and 85% CO selectivity: (a) total system efficiency η_{th}, and water balance, and (b) subsystem efficiencies η_{FP}, η_{FC}, and η_{BOP}.

also leads to higher anode CO overpotentials and increased parasitic loads. The drop of V_{cell} by 0.1 V between half and full power demonstrates the impact of both higher current densities and anode inlet CO concentrations on system efficiency.

Table 4.3: Key system states and outputs for net powers $\dot{W}_{net}$=2500 W and 5000 W, and CO tolerance factors ξ_{CO}=1 and 5 at baseline conditions.

Parameter	**Value**			
Net power $\dot{W}_{net}$ / W	2500	5000	2500	5000
Anode CO tolerance factor ξ_{CO}	1	1	5	5
Overall system efficiency η_{th}	0.295	0.246	0.298	0.278
Individual cell voltage V_{cell} / V	0.767	0.667	0.775	0.737
Average current density i / A·cm^2	0.182	0.410	0.181	0.367
Gross power demand $\dot{W}_{gross}$ / W	3149	6148	3147	6082
WGS reactor conditions:				
Outlet temperature T_{WGS} / °C	253	368	252	356
Outlet H_2 mole fraction	0.393	0.372	0.393	0.376
Outlet CO mole fraction	0.0327	0.0541	0.0327	0.0503
PROx reactor conditions				
Outlet temperature after cooling / °C	60	79	60	72
Outlet H_2 mole fraction	0.362	0.324	0.325	0.331
Outlet CO concentration / ppm	23.3	92.7	23.1	76.2

The complex interactions affecting overall system performance can be grouped into subsystems associated with the fuel processing and purification (η_{FP}), the fuel cell stack (η_{FC}), and the balance of plant (η_{BOP}). The equations for each of these efficiencies are provided in Equations 4.2-4.4. η_{FP} is the ratio of combustion enthalpy in the H_2 exiting the PROx reactor and entering the fuel cell stack to the combustion enthalpy of the hydrocarbon fuel consumed to produce the H_2. The fuel cell stack efficiency η_{FC} is the power produced by the fuel cell divided by the combustion enthalpy of the H_2 entering the stack, including non-utilized H_2. Since the stoichiometric ratio (of H_2 flow to H_2 consumed in the anode) is fixed at 1.3 in this study, the mass flow of H_2 into the anode is proportional to the current density. Thus, Equation 4.3 can also be written in terms of cell voltage V_{cell} and the constant fuel cell utilization $\varepsilon_{H_2,FC}$. Finally, the balance of plant efficiency η_{BOP} is the ratio of usable net power to the total power produced. It is readily seen that the product of Equations 4.2-4.4 produces the overall system efficiency η_{th} of Equation 4.1.

$$\eta_{FP} = \frac{\dot{m}_{H_2,anode\ in} h_{H_2,comb}}{\dot{m}_{HC,in} h_{HC,comb}} \tag{4.2}$$

$$\eta_{FC} = \frac{n_{cells} A_{cell} i V_{cell}}{\dot{m}_{H_2,anode\ in} h_{H_2,comb}} = \frac{\varepsilon_{H_2,FC} 2F \bar{W}_{H_2} V_{cell}}{h_{H_2,comb}} \tag{4.3}$$

$$\eta_{BOP} = \frac{n_{cells} A_{cell} i V_{cell} - \dot{W}_{lost}}{n_{cells} A_{cell} i V_{cell}} \tag{4.4}$$

Figure 4.2b shows the breakdown of the three subsystem efficiencies for the full and half power cases shown in Figure 4.2a. Increasing from half to full power results in significant decreases in η_{FP} and η_{FC}, and slight gains in η_{BOP}. The decrease in η_{FP} with increasing $\dot{W}_{net}$ arises from the increased WGS outlet temperature T_{WGS}, and thus lower H_2 (and higher CO) equilibrium outlet mold fractions as indicated in Table 4.3. The correlation between $\dot{W}_{net}$ and T_{WGS} occurs because both ATR and WGS reactor heat losses (driven by both radiation and natural convection) do not scale proportionally with reactor flow rates. As power demand, fuel consumption, and T_{WGS} increase, the associated higher CO concentrations exiting the WGS also lead to increased parasitic H_2 consumption in the PROx reactor, which causes further decreases in η_{FP} with increasing $\dot{W}_{net}$. These effects could be mitigated by adjusting the S/C up and O/C down at higher power conditions to obtain higher

H_2 mole fractions out of the WGS reactor, but such control strategies are outside the scope of this study, where S/C and O/C remained fixed.

The higher levels of CO exiting the WGS and PROx reactor with increasing $\dot{W}_{net}$ also result in lower V_{cell} and η_{FC} as seen in Table 4.3 and Figure 4.2b. Since balance of plant components are sized to meet maximum load and are generally more efficient at full power output conditions, the increased η_{BOP} at full power can offset some of the losses in η_{FP} and η_{FC}. However, Figure 4.2b also shows that at higher T_{amb}, parasitic loads associated with the coolant loop fan grow substantially at the full power condition and cause η_{BOP} to fall. Since η_{FP} and η_{FC} are largely unaffected by T_{amb}, the larger drop in η_{BOP} at full power is responsible for the steeper decline of η_{th} at higher T_{amb}.

The first exploration of the effects of enhanced CO tolerance involved rerunning the cases of Figure 4.2 with the same PROx reactor settings but with a 5X increase in the anode electrocatalyst CO tolerance, ξ_{CO}. The system performance results with 5X enhanced CO tolerance are illustrated in Figure 4.3. With PROx parameters held at the same baseline, the increased CO tolerance primarily serves to raise V_{cell} and thus η_{FC}, as can be seen in Table 4.3 and by comparing Figures 4.2 and 4.3. The impact of CO tolerance is much more significant at full power conditions where CO anode overpotentials are larger; η_{FC} jumps from 41.0% at ξ_{CO}=1 to 45.2% at ξ_{CO}=5 at T_{amb}=30 °C. On the other hand, at half power the stack is operating in the high voltage, low current density region of the curves shown in Figure 3.3, where CO overpotentials are already small, and so there is significantly less improvement with increasing ξ_{CO} — η_{FC} goes from 47.1% to 47.6% at T_{amb}=30 °C. η_{FP} and

η_{BOP} are only affected indirectly, as the higher η_{FC} reduces fuel consumption and parasitic demands. In general, over the entire T_{amb} range, increasing ξ_{CO} from 1 to 5 (at baseline PROx reactor conditions) raises η_{th} by 3% or more at full power and only 0.3% at half power. The water balance remains largely unchanged with the increase in ξ_{CO}.

4.2.2 Net Power

Next the net power demand was varied from 1000 W to 5000 W to explore how the trends observed above translate over a broader range of power conditions. Figure 4.4a plots η_{th} and T_{WGS} versus $\dot{W}_{net}$ at T_{amb}=30 °C for both ξ_{CO}=1 and 5, clearly showing the increase in T_{WGS} as power demand and fuel consumption grow. Increased T_{WGS} leads to lower H_2 mole fractions and higher CO levels from the fuel processor as discussed earlier. The resulting decline in η_{FP} and η_{FC} is shown in the plot of subsystem efficiencies in Figure 4.4b. V_{cell} and η_{FC} also fall as increasing power pushes the stack to higher current densities, independent of CO effects. These decreases are offset by a rise in η_{BOP} as $\dot{W}_{net}$ increases, with the net effect that η_{th} peaks near 3000 W net electric output. Resizing of components such as the fuel cell stack or cathode or ATR air compressors may shift the optimal efficiency, but component size effects on system performance are not studied here. As before, enhanced CO tolerance has a large effect on η_{FC} at higher powers, and only indirectly raises the other two subsystem efficiencies. Below half power improvements in η_{th} are insignificant since the high baseline PROx conversion limits CO overpotentials

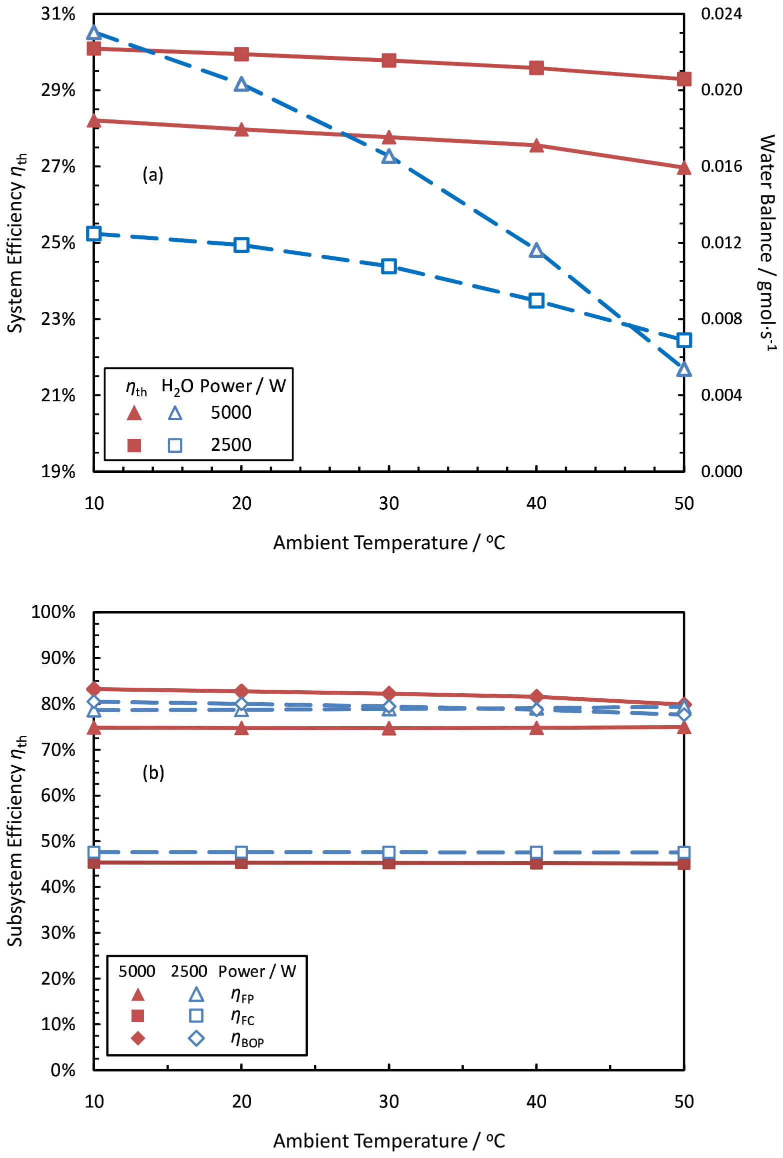

Figure 4.3: PEM fuel cell system performance versus T_{amb} at full and half power at 5X the baseline CO tolerance (ξ_{CO}=5) and PROx reactor performance at 99% CO conversion and 85% CO selectivity: (a) total system efficiency η_{th}, and water balance, and (b) subsystem efficiencies η_{FP}, η_{FC}, and η_{BOP}.

and the impact of CO tolerance. A reduced PROx CO conversion would cause the effects of increased ξ_{CO} to be more significant at lower power conditions.

At the baseline CO tolerance, Figure 4.4 shows that η_{FP} and η_{FC} are relatively flat below $\dot{W}_{net}$=3000 W. This is due to temperatures in the WGS reactor reaching the equilibrium temperature limit of 300 °C below which no further improvements to the H_2 mole fractions out of the WGS are achievable within the assumed kinetic limits of the WGS reactor. This is illustrated in Figure 4.5, which plots anode inlet CO concentration against T_{WGS} for the range of power conditions and ξ_{CO}=1 and 5. T_{WGS} is the outlet temperature of the last stage of the WGS reactor. However at T_{WGS} <300 °C previous stages may still be active, thus the decreasing CO concentrations even below T_{WGS} =300 °C). As T_{WGS} increases above 300 °C the amount of CO entering the fuel cell anode increases sharply. This rise in CO concentrations is accompanied by a drop in V_{cell}, as also shown in Figure 4.5. The results emphasize the importance of optimizing WGS performance, as well as the potential for improved CO-tolerant anode electrocatalysts to reduce demands on the WGS reactor (in terms of size) and perhaps also the PROx reactor as discussed further below.

To explore the effects of power demand and ξ_{CO} on the balance of plant more fully, the specific parasitic power demands for the system at baseline and 5X-increased anode CO tolerance at full and half power are shown in Figure 4.6. In general, the total parasitics $\dot{W}_{lost}$ for full and half power for the different CO tolerances are less than 20% of net power out. The results in Figure 4.6 show that the largest parasitic losses come from the cathode and fuel processor (FP) compressors. The radiator fan power demand increases with T_{amb}, rising sharply as T_{amb}

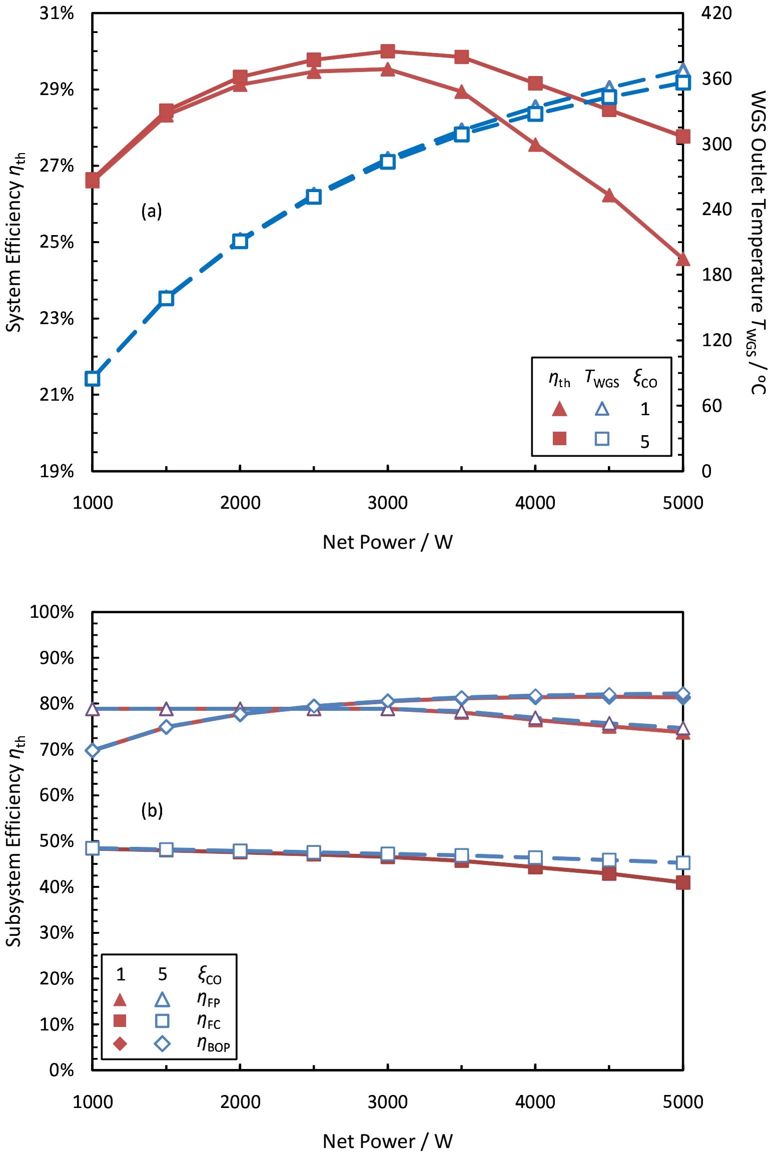

Figure 4.4: PEM fuel cell system performance versus $\dot{W}_{net}$ at ξ_{CO}=1 and ξ_{CO}=5 with PROx reactor performance at 99% CO conversion and 85% CO selectivity: (a) η_{th} and T_{WGS}, and (b) subsystem efficiencies η_{FP}, η_{FC}, and η_{BOP}.

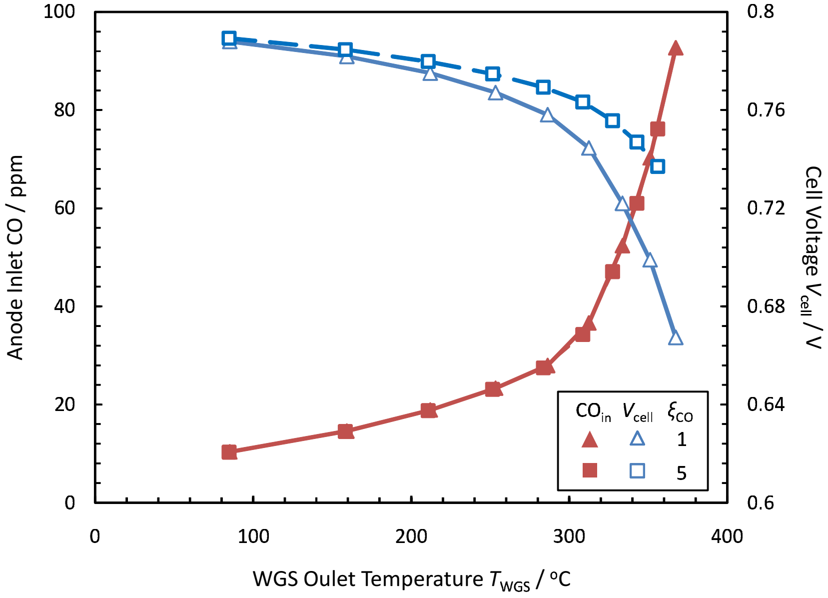

Figure 4.5: Anode inlet CO concentration and V_{cell} versus T_{WGS} at T_{amb}=30 °C for baseline and 5X baseline CO tolerances with PROx reactor conditions are 99% Co conversion and 0.85 CO selectivity.

approaches the temperature of the coolant such that the fan must push significantly more air through the coils to achieve adequate cooling for the coolant loop and the exhaust condenser. Parasitic loads do not scale linearly with net power, resulting in lower η_{BOP} at the half power condition as discussed above.

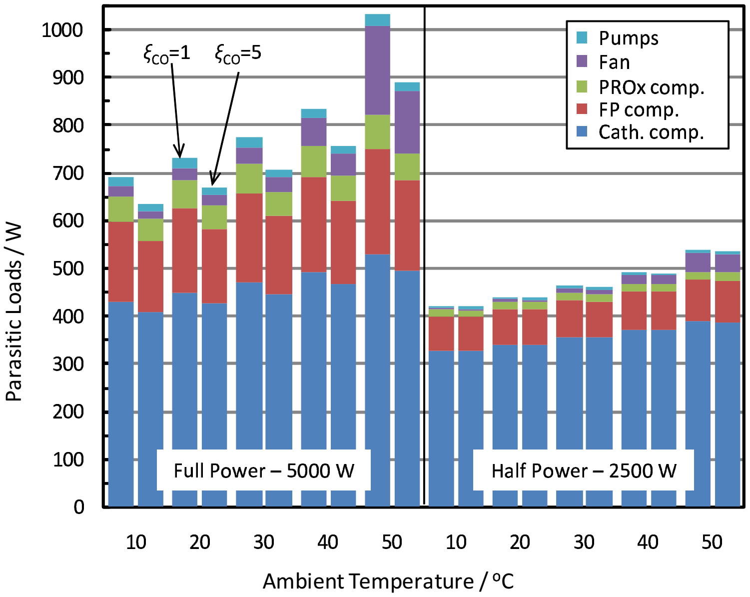

Figure 4.6: Comparison of parasitic loads at full and half power for a range of T_{amb} at ξ_{CO}=1 (left bar of each pair) and ξ_{CO}=5 (right bar of each pair). PROx reactor conditions at 0.99 CO conversion and 0.85 CO selectivity.

4.2.3 PROx CO Selectivity

The results from Figures 4.2-4.6 suggest that increasing CO tolerance provides significant improvements in overall system performance only at conditions where anode CO overpotentials are relatively large. However, in the cases investigated so far CO concentrations have remained below 100 ppm, causing CO overpotentials less than 85 mV. This is because the baseline PROx conditions of 99% CO conversion and 85% CO selectivity represent an extremely high performance reactor. Obtaining such high performance may require large, expensive multi-stage reactors and heat exchangers for fine temperature control. As such, the model was used to explore whether increased CO tolerance might allow for less expensive PROx reactors with either reduced conversion (smaller size) and/or reduced selectivity (less expensive catalysts).

The first parametric study involved changing PROx CO selectivity while keeping PROx CO conversion high at 99%. Increasing selectivity reduces H_2 consumption in the PROx, raising η_{FP} since less fuel is required to supply the same amount of H_2 to the stack. η_{BOP} also increases as the PROx air compressor demand falls. These combined effects are illustrated in Figure 4.7, where η_{th} increases as the CO selectivity goes from 0.75 to 1, mainly due to a rise in η_{FP} from 71.8% to 75.9% at ξ_{CO}=1. Over the entire range of PROx CO selectivities investigated here, a 5X improvement in CO tolerance raises η_{th} by 3–4% points at full power. As discussed earlier, gains with increased ξ_{CO} are due principally to improvements in V_{cell} and η_{FC}.

PROx CO selectivity does not have a large impact on anode CO concentrations, which at the high PROx CO conversion of 99% are relatively low (<100 ppm) and only decline slightly with higher CO selectivities as efficiencies go up and fuel flow decreases. Figure 4.7 demonstrates that improvements in anode CO tolerance have a larger impact on system efficiency than increased PROx CO selectivity alone at high PROx CO conversions. However if the CO conversion were reduced from

99%, reformer efficiencies would see large drops at lower CO selectivities as much more H_2 was consumed in the PROx. Even at the high 99% CO conversion, η_{th} is a relatively strong function of CO selectivity, showing the value in continued research activity to developed improved, reliable PROx catalysts.

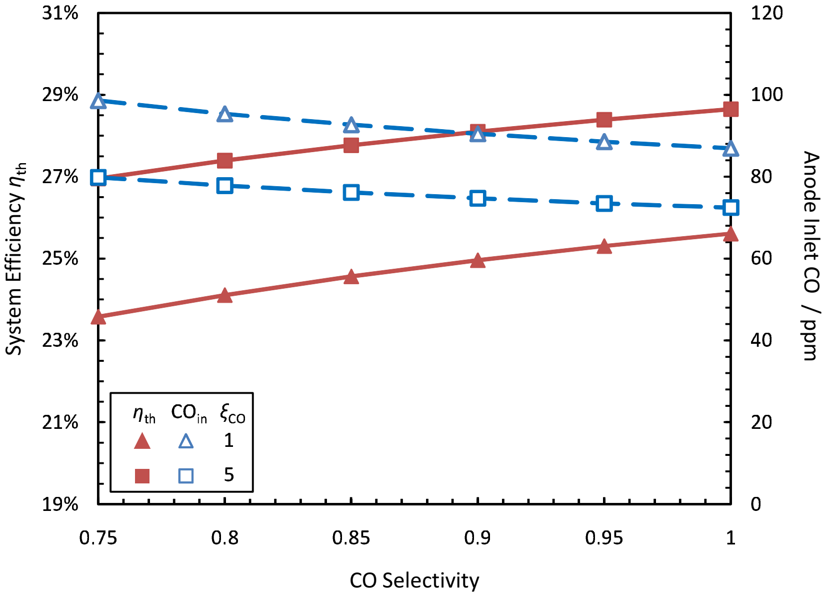

Figure 4.7: Full power η_{th} and anode inlet CO ppm at T_{amb}=30 °C for varying PROx reactor CO selectivities with constant PROx reactor CO conversion of 0.99, at baseline and 5X baseline CO tolerances.

4.2.4 PROx CO Conversion

Changes in PROx selectivity require changes in catalyst composition, but changes in PROx CO conversion can be accomplished with only changes in catalyst loading and thus may be a straightforward means of impacting system performance and/or cost. A reduced PROx catalyst loading may allow for fewer PROx reactor stages and reduced system cost and size. To explore how potential improvements in CO tolerance of anode electrocatalysts can reduce the demand for high PROx conversions while maintaining adequately high η_{th}, ξ_{CO} was varied from 1 to 10 for two different PROx CO conversions (the baseline 99% and a reduced 90%).

At half power output conditions the high baseline PROx conversion of 99% shows very minor improvements in η_{th} with increased ξ_{CO}. When the PROx reactor is shrunk such that CO conversion is only 90%, η_{th} drops by more than 2% points from 29.5% to 27.1%. However, increasing ξ_{CO} to higher values reduces this penalty for the reduced PROx conversion at half power, such that by ξ_{CO}= 5, the drop in η_{th} is less than 0.5% points from 29.8% to 29.4% and by ξ_{CO}=10, the drop in η_{th} is less than 0.1% points. These improvements in performance, which are principally due to improvements in η_{FC}, illustrate one of the real system values in improving anode CO tolerance: higher fuel cell CO tolerance allows for reduction in demands for PROx-based CO cleanup as studied here, which can mean smaller, less complex reactors with lower CO conversion.

The value of higher ξ_{CO} in allowing lower PROx reactor performance is further illustrated in Figure 4.8a by plotting η_{th} as well as anode inlet CO concentrations for full power conditions with PROx CO conversions of 90 and 99%. The improvements in η_{th} with increased CO tolerance for both PROx CO conversions are much more dramatic at the full power conditions because the higher anode overpotentials offer more opportunity for increasing V_{cell} and η_{FC} with higher ξ_{CO}. For the baseline 99% conversion, η_{th} at full power increases significantly (by 3.0% points) up to $\xi_{CO} = 5$ and less so as ξ_{CO} increases beyond 5. This is in large part because the <100 ppm

CO levels entering the anode at the high PROx conversion are largely insensitive to ξ_{CO}. Thus, there is limited margin for further improvement at the highest values of ξ_{CO} studied. On the other hand, for the reduced (90%) PROx CO conversion cases, increases in η_{th} with ξ_{CO} remain large even up to ξ_{CO}=10. This is in part because the lower CO conversion results in quite high CO concentrations entering the anode, and these concentrations drop dramatically as ξ_{CO} rises. In fact, the CO concentrations become so high (>2000 ppm) at the baseline ξ_{CO} for PROx conversion of 90% that the fuel cell system is unable to produce the full power $\dot{W}_{net}$=5000 W, as indicated by no point for this case in Figure 4.8a. However, for ξ_{CO}=2, η_{th} approaches 20% with the reduced PROx conversion and this values rises significantly to 25% as ξ_{CO} is increased to 10. This is largely due to significant improvements in η_{FC} under these conditions where CO overpotentials at the baseline conditions are exceptionally large without the enhanced anode CO tolerance. V_{cell} is 0.557 V at the ξ_{CO}=2 condition and rises to a much more acceptable value of 0.670 V at ξ_{CO}=10 for the 90% PROx conversion cases. The impact of ξ_{CO} on η_{FC} is illustrated in Figure 4.8b which breaks down the subsystem efficiencies and shows the significant increase in η_{FC} with ξ_{CO} for the lower PROx CO conversion cases. It is noteworthy that the significant improvement in η_{FC} also results in smaller improvements in both η_{FP} and η_{BOP} by reducing the compressor and fan flow requirements and by also improving the WGS outlet equilibrium with lower CO and higher H_2 concentrations. These results clearly indicate that the value of improved anode CO tolerance is tightly linked to the performance of the PROx reactor. As such, the advantages of enhanced CO tolerance depend on the system and its range of operating conditions.

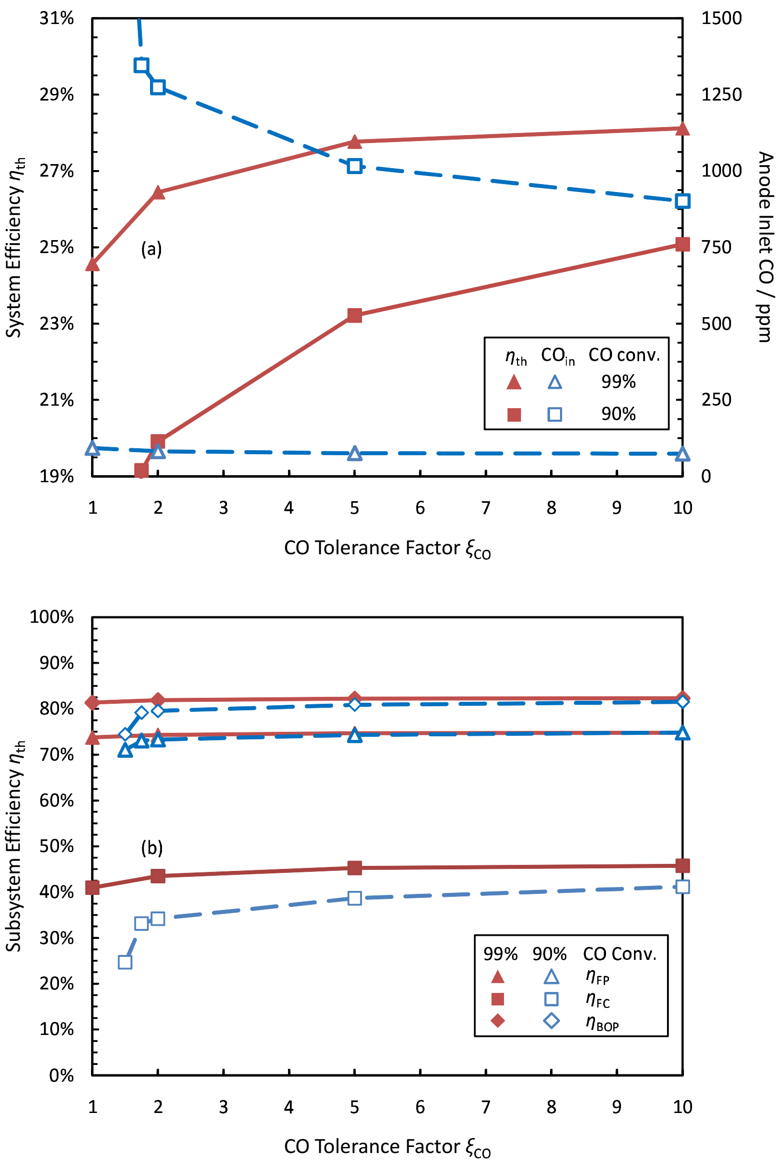

Figure 4.8: PEM fuel cell system performance versus anode electrocatalyst CO tolerance ξ_{CO} at full power for PROx reactor conditions of 90% and 99% CO conversion at a constant CO selectivity of 0.85: (a) total system efficiency η_{th} and anode inlet CO ppm, and (b) subsystem efficiencies η_{FP}, η_{FC}, and η_{BOP}.

Chapter 5

Conclusions

This study examined the possibility of PtMo nano-structured electrocatalysts for improved CO tolerance in low-temperature PEM fuel cell anodes and then explored system-level impacts through modeling of enhanced PEM fuel cell anode catalysts.

The experimental investigation of nano-architectured anode electrocatalysts built on previous work that suggested high CO tolerance of Pt-Mo anode electrocatalysts in thin-film RDE experiments. MEAs incorporating the promising PtMo alloy and MoO_x@Pt core-shell catalysts were fabricated and tested in pure H_2 and CO concentrations up to 1000 ppm, and multi-day stability testing was also conducted. Performance was compared against a commercial PtRu MEA as well as an in-house fabricated MEA using commercial PtRu catalyst.

A companion modeling study explored the benefits of improving anode CO tolerance on the system performance of a liquid-hydrocarbon-fueled PEM fuel cell generator using a PROx reactor for reformate clean-up. A system model was built which included empirical curves for baseline CO tolerance based on the PtMo anode catalysts tested in the experimental portion of this study. A CO tolerance factor was defined which shifted the polarization effects of CO to higher ppm values. The system model provided a basis for exploring the interactions between CO tolerance of the anode and PROx operating conditions.

5.1 Significant Results

5.1.1 CO Tolerance of Nano-architectured Pt-Mo Electrocatalysts

MEAs were successfully fabricated with performance on pure H_2 fuel reaching 0.9 $W{\cdot}cm^{-2}$ for the PtRu alloy. Testing of PtMo and MoO_x@Pt MEAs demonstrated the superior CO tolerance of the alloy, which exhibited a voltage drop of only 95 mV in 100 ppm CO at 0.5 $A{\cdot}cm^{-2}$, compared to drops of 230 mV for PtRu and 260 mV for the core-shell electrocatalyst. However the pure H_2 polarization curves for both Mo-containing catalysts suggested high activation overpotentials and poor catalyst utilization, and the CO tolerance of MoO_x@Pt MEAs was significantly lower than predicted by RDE results.

Bulk resistance measurements indicated that although the MEA fabrication process was repeatable, changes in the catalyst ink composition were found to influence the resulting catalyst layer performance. Thus, it is reasonable to suspect that the low exchange current densities and utilizations of the Mo-containing catalysts are related to the varying surfactants and heat-treatments applied to the catalysts and subsequent effects on the catalyst ink consistency.

Despite relatively poor performance on a total catalyst loading basis, the MoO_x@Pt electrocatalyst displays more comparable behavior on a precious metal loading basis, with superior performance to PtRu at 25 ppm of CO. PtMo and MoO_x@Pt MEAs were tested for up to 9 days in H_2 and CO, and held at 0.6 V in 100 ppm of CO for 60 and 72 hours, respectively. The PtMo MEA performance was quite stable at 0.48 A·cm^2 over 60 hours, while the MoO$_x$@Pt current density declined slowly, from 0.22 ·cm^2 to 0.18 ·cm^2 over 60 hours. V-i curves measured during stability testing indicate an increase in η_{CO} and activation overpotentials over testing, possibly due to increasing oxidation of the Mo.

TEM and EDX analysis after stability testing found no significant changes in particle size or elemental composition, however semi-quantitative SEM EDX line scans showed that Mo content in the membrane and cathode increased during testing. This apparent leaching was slightly lower for the MoO$_x$@Pt particles than for the PtMo, offering hope of increased long-term stability from core-shell architectures.

5.1.2 Model

For the system illustrated in Figure 4.1 with operating parameters described in Table 4.2, overall system efficiencies at baseline CO tolerances and state-of-the-art PROx reactor performance (99% CO conversion and 85% CO selectivity) ranged from 24% at full power ($\dot{W}_{net}$ = 5000 W) up to 29.5% at intermediate power conditions ($\dot{W}_{net}$ = 3000 kW). At lower power conditions and higher ambient temperatures, efficiencies dropped off due to increases in the fraction of work required to operate balance-of-plant compressors, fans, and pumps.

Assuming advances in CO tolerant catalysts allowing a 5X reduction in CO penalties compared to current catalysts, model calculations showed that the fuel cell efficiency increased only slightly at the lower power conditions, to 30.0% at $\dot{W}_{net}$=3000 W, but more dramatically at high power conditions, up to 27.8% at $\dot{W}_{net}$=5000 W. In general, conditions for significant improvement in system efficiency with increased anode CO tolerance were those where relatively high current densities and relatively high (>50 ppm) anode inlet CO concentrations caused large anode overpotentials that were reduced with improved CO-tolerant anode electrocatalysts. Improvement in fuel cell voltages and efficiencies with increased CO tolerance also had additional system benefits such as small reductions in parasitic loads which further increased system efficiencies.

Furthermore, increased fuel cell CO tolerance permitted significantly lower PROx CO selectivities and CO conversions without the significant penalties in overall system efficiency observed at baseline tolerance.

5.2 Recommendations for Future Work

The catalyst inks and MEA fabrication procedures employed in this study were not fully optimized. Nonetheless, the MoO_x@Pt and PtMo electrocatalysts demonstrated comparable and improved CO tolerance of relative to PtRu, and RDE tests indicate that much higher performance is possible. Future tests should aim to capture the great potential of both Mo-containing electrocatalysts for high CO tolerance. Low catalyst utilizations suggest that there are improvements to be made in the catalyst layer, whether through modified post-synthesis treatments to fully remove surfactants, or changes to the catalyst ink composition and ink application method.

Given the apparently reduced active surface areas of the two Mo-containing catalysts, especially MoO_x@Pt, more meaningful comparison of the catalysts should be conducted on a metal loading or active surface area basis. This will require measurement of exact metal loading in the active area, which can be accomplished through inductively coupled plasma mass spectrometry or neutron activation analysis. Electrochemically active surface areas of the catalysts can be determined using cyclic voltammetry. Awareness of catalyst utilizations in the MEAs would also be useful while optimizing catalyst layer fabrication protocols.

Conclusive determination of catalyst stability will require testing over much longer time periods than the 9 days reached in this work. In future post-testing analysis, XPS and XRD should be used to determine if any structural changes take place during testing, and possibly to examine oxidation states of the Mo.

As improved CO tolerance is demonstrated by the MoO_x@Pt or other electrocatalysts, further modeling work should seek opportunities for reducing system costs with smaller PROx or WGS reactors as well as smaller fuel cell stacks. Such a study may offer direction in development efforts for PEM fuel cell systems with CO-tolerant anodes in order to compete more effectively for portable and/or distributed power applications involving liquid hydrocarbon fuels.

Also, as progress is made in the assembly and testing of the working system prototype, component models should continue to be refined and validated to closely approximate real word performance.

Bibliography

[1] Kang, I., Bae, J., Yoon, S., and Yoo, Y. *Journal of Power Sources* **172**(2), 845–852 October (2007).

[2] Cheng, X., Shi, Z., Glass, N., Zhang, L., Zhang, J. J., Song, D. T., Liu, Z. S., Wang, H. J., and Shen, J. *Journal of Power Sources* **165**(2), 739–756 March (2007).

[3] Smitha, B., Sridhar, S., and Khan, A. A. *Journal of Membrane Science* **259**(1-2), 10–26 August (2005).

[4] Li, Q., Jensen, J. O., Savinell, R. F., and Bjerrum, N. J. *Progress in Polymer Science* **34**(5), 449–477 May (2009).

[5] Oetjen, H. F., Schmidt, V. M., Stimming, U., and Trila, F. *Journal of The Electrochemical Society* **143**(12), 3838–3842 December (1996).

[6] Mukerjee, S., Urian, R. C., Lee, S. J., Ticianelli, E. A., and McBreen, J. *Journal of The Electrochemical Society* **151**(7), A1094–A1103 (2004).

[7] Gu, T., Lee, W. K., Zee, J. W. V., and Murthy, M. *Journal of The Electrochemical Society* **151**(12), A2100–A2105 (2004).

[8] Enback, S. and Lindbergh, G. *Journal of The Electrochemical Society* **152**(1), A23–A31 (2005).

[9] Uribe, F. A., Valerio, J. A., Garzon, F. H., and Zawodzinski, T. A. *Electrochemical and Solid-State Letters* **7**(10), A376–A379 (2004).

[10] Carrette, L. P. L., Friedrich, K. A., Huber, M., and Stimming, U. *Physical Chemistry Chemical Physics* **3**(3), 320–324 (2001).

[11] Zhang, J. *Investigation of CO Tolerance in Proton Exchange Membrane Fuel Cells.* PhD thesis, Worcester Polytechnic Institute, June (2004).

[12] Pereira, L. G. S., Paganin, V. A., and Ticianelli, E. A. *Electrochimica Acta* **54**(7), 1992–1998 February (2009).

[13] Urian, R. C., Gulla, A. F., and Mukerjee, S. *Journal Of Electroanalytical Chemistry* **554**, 307–324 September (2003).

[14] Leng, Y. J., Wang, X., and Hsing, I. M. *Journal Of Electroanalytical Chemistry* **528**(1-2), 145–152 June (2002).

[15] Lim, D. H., Choi, D. H., Lee, W. D., and Lee, H. I. *Applied Catalysis B: Environmental* **89**(3-4), 484–493 July (2009).

[16] Arenz, M., Stamenkovic, V., Blizanac, B. B., Mayrhofer, K. J. J., Markovic, N. M., and Ross, P. N. *Journal of Catalysis* **232**(2), 402–410 June (2005).

[17] Mukerjee, S., Lee, S. J., Ticianelli, E. A., McBreen, J., Grgur, B. N., Markovic, N. M., Ross, P. N., Giallombardo, J. R., and Castro, E. S. D. *Electrochemical and Solid-State Letters* **2**(1), 12–15 (1999).

[18] Ioroi, T., Akita, T., Yamazaki, S., Siroma, Z., Fujiwara, N., and Yasuda, K. *Electrochimica Acta* **52**(2), 491–498 October (2006).

[19] Lebedeva, N. P. and Janssen, G. J. M. *Electrochimica Acta* **51**(1), 29–40 October (2005).

[20] Martinez-Huerta, M. V., Rodriguez, J. L., Tsiouvaras, N., Pena, M. A., Fierro, J. L. G., and Pastor, E. *Chemistry of Materials* **20**(13), 4249–4259 July (2008).

[21] dos Anjos, D. M., Kokoh, K. B., Lger, J., Andrade, A., Olivi, P., and Tremiliosi-Filho, G. *Journal of Applied Electrochemistry* **36**(12), 1391–1397 December (2006).

[22] Papakonstantinou, G., Paloukis, F., Siokou, A., and Neophytides, S. G. *Journal of The Electrochemical Society* **154**(10), B989–B997 October (2007).

[23] Mikhailova, A. A., Pasynskii, A. A., Dobrokhotova, Z. V., Grinberg, V. A., and Khazova, O. A. *Russian Journal of Electrochemistry* **44**(3), 303–312 March (2008).

[24] Adzic, R. R., Zhang, J., Sasaki, K., Vukmirovic, M. B., Shao, M., Wang, J. X., Nilekar, A. U., Mavrikakis, M., Valerio, J. A., and Uribe, F. *Topics in Catalysis* **46**(3-4), 249–262 December (2007).

[25] Liu, Z., Hu, J. E., Wang, Q., Gaskell, K., Frenkel, A. I., Jackson, G. S., and Eichhorn, B. *Journal of the American Chemical Society* **131**(20), 6924–6925 May (2009).

[26] Schumacher, N., Andersson, K., Grabow, L. C., Mavrikakis, M., Nerlov, J., and Chorkendorff, I. *Surface Science* **602**(3), 702–711 February (2008).

[27] Alayoglu, S., Nilekar, A. U., Mavrikakis, M., and Eichhorn, B. *Nature Materials* **7**(4), 333–338 March (2008).

[28] Castaldi, M. J. and Barrai, F. *Catalysis Today* **129**(3-4), 397–406 December (2007).

[29] Specchia, S., Cutillo, A., Saracco, G., and Specchia, V. *Industrial & Engineering Chemistry Research* **45**(15), 5298–5307 July (2006).

[30] Kamarudin, S. K., Daud, W. R. W., Som, M. A., Takriff, M. S., and Mohammad, A. W. *Journal of Power Sources* **157**(2), 641–649 July (2006).

[31] Zhu, W. H. H., Payne, R. U., and Tatarchuk, B. J. *Journal of Power Sources* **156**(2), 512–519 June (2006).

[32] Lattner, J. R. and Harold, M. P. *International Journal of Hydrogen Energy* **29**(4), 393–417 March (2004).

[33] Ahmed, S., Kopasz, J., Kumar, R., and Krumpelt, M. *Journal of Power Sources* **112**(2), 519–530 November (2002).

[34] Biesheuvel, R. M. and Kramer, G. J. *Journal of Power Sources* **138**(1-2), 156–161 November (2004).

[35] Doss, E. D., Kumar, R., Ahluwalia, R. K., and Krumpelt, M. *Journal of Power Sources* **102**(1-2), 1–15 December (2001).

[36] Ahluwalia, R. K., Doss, E. D., and Kumar, R. *Journal of Power Sources* **117**(1-2), 45–60 May (2003).

[37] Pearlman, J. B., Bhargav, A., Shields, E. B., Jackson, G. S., and Hearn, P. L. *Journal of Power Sources* **185**(2), 1056–1065 December (2008).

[38] Wilson, M. S., Valerio, J. A., and Gottesfeld, S. *Electrochimica Acta* **40**(3), 355–363 February (1995).

[39] Bender, G., Zawodzinski, T. A., and Saab, A. P. *Journal of Power Sources* **124**(1), 114–117 October (2003).

[40] Xiong, L. and Manthiram, A. *Electrochimica Acta* **50**(16-17), 3200–3204 May (2005).

[41] Barrio, A., Bae, J. S., Lombrana, J. I., Uresandi, M., and Mijangos, F. *International Journal of Chemical Reactor Engineering* **6** (2008).

[42] Sasikumar, G., Ihm, J. W., and Ryu, H. *Electrochimica Acta* **50**(2-3), 601–605 November (2004).

[43] Tang, H., Wang, S., Jiang, S. P., and Pan, M. *Journal of Power Sources* **170**(1), 140–144 June (2007).

[44] Gamburzev, S. and Appleby, A. J. *Journal of Power Sources* **107**(1), 5–12 April (2002).

[45] Zhang, J., Thampan, T., and Datta, R. *Journal of The Electrochemical Society* **149**(6), A765–A772 June (2002).

[46] Iyuke, S. E., Mohamad, A. B., Kadhum, A. A. H., Daud, W. R. W., and Rachid, C. *Journal of Power Sources* **114**(2), 195–202 March (2003).

[47] Zhang, H., Wang, X., Zhang, J., and Zhang, J. In *PEM Fuel Cell Electrocatalysts and Catalyst Layers*, 889–916. Springer London (2008).

[48] Brosha, E. and Pivovar, B. March (2008).

[49] Schonert, M., Jakoby, K., Schlumbohm, C., Glsen, A., Mergel, J., and Stolten, D. *Fuel Cells* **4**(3), 175–179 (2004).

[50] Gasteiger, H. A., Kocha, S. S., Sompalli, B., and Wagner, F. T. *Applied Catalysis B: Environmental* **56**(1-2), 9–35 March (2005).

[51] Shao, Y. Y., Yin, G. P., and Gao, Y. Z. *Journal of Power Sources* **171**(2), 558–566 September (2007).

[52] Coloma, F., Prado-Burguete, C., and Rodriguez-Reinoso, F. *Studies in Surface Science and Catalysis* **75**(3), 2103–2106 (1993).

[53] Wang, Z. B., Yin, G. P., and Shi, P. F. *Carbon* **44**(1), 133–140 (2006).

[54] Abe, H., Matsumoto, F., Alden, L. R., Warren, S. C., Abrua, H. D., and DiSalvo, F. J. *Journal of the American Chemical Society* **130**(16), 5452–5458 April (2008).

[55] Stoffels, E., Stoffels, W. W., Ceccone, G., Hasnaoui, R., Keune, H., Wahl, G., and Rossi, F. *Journal of Applied Physics* **86**(6), 3442–3451 (1999).

[56] Sasaki, K., Watanabe, K., and Teraoka, Y. *Journal of The Electrochemical Society* **151**(7), A965–A970 July (2004).

[57] Maeda, N., Matsushima, T., Uchida, H., Yamashita, H., and Watanabe, M. *Applied Catalysis A: General* **341**(1-2), 93–97 June (2008).

[58] Berg, P., Novruzi, A., and Promislow, K. *Chemical Engineering Science* **61**(13), 4316–4331 July (2006).